

See discussions, stats, and author profiles for this publication at: <https://www.researchgate.net/publication/357429118>

Alpine subduction zone metamorphism in the Paleozoic successions of the Monti Romani (Northern Apennines, Italy)

Article in *Journal of Metamorphic Geology* · December 2021

DOI: 10.1111/jmg.12650

CITATION

1

READS

277

5 authors, including:



Samuele Papeschi

Japan Agency for Marine-Earth Science Technology

45 PUBLICATIONS 133 CITATIONS

[SEE PROFILE](#)



Federico Rossetti

Università Degli Studi Roma Tre

188 PUBLICATIONS 7,410 CITATIONS

[SEE PROFILE](#)

Some of the authors of this publication are also working on these related projects:



Evolution of the Adria-Europe plate boundary [View project](#)



Tectonometamorphic evolution of the Massa Unit in Punta Bianca area (Northern Apennines, Italy) [View project](#)

Papeschi Samuele (Orcid ID: 0000-0002-5774-7119)
Rossetti Federico (Orcid ID: 0000-0001-8071-7252)

Alpine subduction zone metamorphism in the Paleozoic successions of the Monti Romani (Northern Apennines, Italy)

Samuele PAPESCHI^a, Alessio PONTESILLI^b, Claudia ROMANO^c, Federico ROSSETTI^{c*} &
Thomas THEYE^d

a. Kochi Institute for Core Sample Research, Institute for Extra-cutting-edge Science and
Technology Avant-garde Research (X-star), JAMSTEC, Japan

b. Istituto Nazionale di Geofisica e Vulcanologia, Roma, Italy

c. Dipartimento di Scienze, Sezione di Scienze Geologiche, Università Roma Tre, Roma, Italy

d. Institut für Anorganische Chemie, Universität Stuttgart, Stuttgart, Germany

***Corresponding author**

Dipartimento di Scienze, Università Roma Tre

Sezione Scienze Geologiche

Largo San Leonardo Murialdo, 1

00146 Roma (Italy)

e-mail: federico.rossetti@uniroma3.it

Tel.: +39 06 5488 8043

This article has been accepted for publication and undergone full peer review but has not been through the copyediting, typesetting, pagination and proofreading process which may lead to differences between this version and the Version of Record. Please cite this article as doi: 10.1002/jmg.12650

Abstract

The hinterland of the Cenozoic Northern Apennines fold-and-thrust belt exposes the metamorphic roots of the chain, vestiges of the subduction-related tectono-metamorphic evolution that led to the buildup of the Alpine orogeny in the Mediterranean region. Like in other peri-Mediterranean belts, the tectono-metamorphic evolution of the Paleozoic continental basement in the Apennines is still poorly constrained, hampering the full understanding of their Alpine orogenic evolution. We report the first comprehensive tectono-metamorphic study of the low-grade metasedimentary (metapsammite/metapelite) succession of the Monti Romani Complex (MRC) that formed after Paleozoic protoliths and constitutes the southernmost exposure of the metamorphic domain of the Northern Apennines. By integrating fieldwork with microstructural studies, Raman spectroscopy on carbonaceous material and thermodynamic modelling, we show that the MRC preserves a D_1/M_1 Alpine tectono-metamorphic evolution developed under HP-LT conditions (~ 1.0 - 1.1 GPa at $T \sim 400$ °C) during a non-coaxial, top-to-the-NE, crustal shortening regime. Evidence for HP-LT metamorphism is generally cryptic within the MRC, dominated by graphite-bearing assemblages with the infrequent blastesis of muscovite \pm chlorite \pm chloritoid \pm paragonite parageneses, equilibrated under cold paleo-geothermal conditions (~ 10 °C/km). Results of this study allow extending to the MRC the signature of subduction zone metamorphism already documented in the hinterland of the Apennine orogen, providing further evidence of the syn-orogenic ductile exhumation of the HP units in the Apennine belt. Finally, we discuss the possible role of fluid-mediated changes in the reactive bulk rock composition on mineral blastesis during progress of regional deformation and metamorphism at low-grade conditions.

1. Introduction

The Mesozoic-Cenozoic geodynamic evolution of the Mediterranean region is dominated by consumption of the Tethyan oceanic realms in the framework of the Mesozoic – Cenozoic convergence between the African and Eurasian plates. The subduction dynamics controlled the mode and the space-time distribution of the Alpine orogenic construction and collapse along convergence zones, during the transition from crustal thickening to thinning in back-arc domains (e.g., Dewey, 1988; Malinverno & Ryan, 1986; Jolivet & Faccenna, 2000; Faccenna et al., 2004). Studies of the tectono-metamorphic evolution of the exhumed high-pressure-low-temperature (HP-LT) blueschist and eclogite facies metamorphic roots of the Alpine orogens have provided a wealth of key information on convergent plate margins structure and evolution (e.g., Ernst, 1971; Ernst and Dal Piaz, 1978; Platt, 1986; Chopin, 1989; Escher & Beaumont, 1997; Jolivet et al., 2003; Rubatto & Herman, 2001; Ring & Layer, 2003; Yamato et al., 2007; Agard et al., 2006; 2009; 2018; Malusà et al., 2015; Penniston-Dorland et al., 2015), deformation mechanisms (e.g., Angiboust et al., 2011; Agard et al., 2018; Locatelli et al., 2018; Kotowski & Behr, 2019; Giuntoli & Viola, 2021), and fluid transport in the lithosphere (Rubatto & Hermann, 2003; Frezzotti et al., 2011; Scambelluri et al., 2015; Maggi et al., 2014; Cook-Kollars et al., 2014; Bebout & Penniston-Dorland, 2016; Lefeuvre et al., 2020; Epstein et al., 2020).

In exhumed metasedimentary units, metamorphic parageneses indicative of HP-LT conditions are generally subtle or cryptic compared to metabasic rocks and susceptible to alteration during retrograde metamorphism or a later thermal overprint. Moreover, metapelites may not always attain chemical equilibrium during low-grade metamorphism, because of, particularly in the case of phengitic muscovite, very slow diffusion rates as well as relatively high nucleation rates (e.g., Worley et al., 1997; Vidal & Parra, 2000; Vidal et al., 2006). Nonetheless, continent-derived metapelitic rocks are common in HP–LT terranes (e.g.,

Goffé & Chopin, 1986; Goffé, et al., 1988; Theye, et al., 1992; Black et al., 1993; Azañon, et al., 1998; Jolivet et al., 1998a, b, 2003; Agard, et al., 2001; Bousquet et al., 2002; Pourteau et al., 2014) and their investigation provides invaluable clues on the tectono-metamorphic evolution of a region (e.g., Goffé et al., 1988; Azañon, et al., 1998; Jolivet et al., 1998a, b, 2003; Agard et al., 2005; Lopez-Carmona et al., 2013, 2014; Lo Pò & Braga, 2014; Di Rosa et al., 2017; Molli et al., 2000; 2018; Pundler et al., 2015; Marrone et al., 2021). This is the case of the metamorphic complexes of the Northern Apennines belt (Figure 1), where the discovery of HP–LT metamorphism is relatively recent with respect to other circum-Mediterranean belts. In the Northern Apennines, Al-rich metapelitic/metapsammitic rocks and related syn-metamorphic veins preserve chloritoid- and carpholite-bearing parageneses that recorded HP–LT metamorphism (Theye et al., 1997; Jolivet et al. 1998b; Giorgetti et al., 1998; Jolivet et al., 1998b; Rossetti et al., 1999; Molli et al., 2000; Brogi & Giorgetti, 2012; Giuntoli & Viola, 2021). This is typical of other Alpine segments like Calabria and the Southern Apennines (Rossetti et al., 2001a; 2004; Iannace et al., 2007; Vitale et al., 2013), the Betic-Rif (Bouybaouene et al., 1995; Azañon et al., 1998; Vidal et al., 1999), Anatolia (Oberhänsli et al., 2001; Pourteau et al., 2014; Plunder et al., 2015), and the Aegean region (Theye et al., 1992; Parra et al., 2002; Cao et al., 2018). In the Northern Apennines, these parageneses largely occur in the Permian-Triassic metasiliciclastic rocks of the Verrucano Group (Jolivet et al., 1998) that, together with low-grade Carboniferous – Permian metamorphics, lay tectonically above a Paleozoic basement that in part registered pre-Alpine Variscan deformation and metamorphism (Paoli et al., 2017; Molli et al., 2020 and references therein). However, the tectono-metamorphic evolution of the low-grade Paleozoic rocks of the Northern Apennines remains poorly defined and uncertainty persists regarding their Alpine structural and thermobaric evolution and the role of Variscan inheritance (Franceschelli et al., 1986, 2004; Conti et al., 1991; Lo Pò & Braga, 2014; Paoli et al., 2017;

Capezzuoli et al., 2021; Molli et al., 2021). Furthermore, the lack of modern quantitative structural, petrological, and geochronological constraints still hampers a full understanding of the Alpine subduction/exhumation history of the region.

In order to refine the Alpine tectono-metamorphic evolution experienced by the Paleozoic metamorphic sequences of the Adria continental crust during orogenic construction, we focus on the Monti Romani metamorphic complex, the southernmost and least studied metamorphic complex of the Northern Apennines (see Curzi et al., 2020; Figure 1a). We constrain, for the first time, HP–LT metamorphic conditions recorded by (Fe, Mg)-chloritoid-bearing assemblages in metapelites. We also document a continuous, syn-metamorphic NE-verging Alpine deformation that we link to underthrusting and nappe stacking during orogenic construction. Our tectono-metamorphic data show that the low-grade Paleozoic rocks of the TMC experienced an Alpine tectono-metamorphic evolution under cold paleo-geothermal conditions (~ 10 °C/km) similar to that documented by the Permian-Triassic siliciclastic rocks of the Verrucano Group in the Northern Apennines, providing further support to the syn-orogenic exhumation of the orogenic roots of the Apennine chain.

2. Geological background

The Northern Apennines formed after the Oligocene, following the Eocene closure of the Ligurian Ocean (Elter et al., 1966, Boccaletti et al., 1971; Alvarez et al., 1974; Elter, 1975; Rossetti et al., 2004; Vitale Brovarone & Herwartz, 2013), a branch of the Neotethys Ocean located between the European margin and the Adria Microplate (Elter & Marroni, 1991; Marroni et al., 2010). In contrast to the Alps, the Northern Apennines (Figure 1a) expose primarily anchizone-facies to low-grade units, tectonically assembled to form a NE-

verging fold-and-thrust belt (Elter et al., 1966; Boccaletti et al., 1971; Patacca & Scandone, 1985; Conti et al., 2020).

The uppermost units of the tectonic pile consist of ophiolite-bearing oceanic and ocean-continent transition units derived from the Ligurian Ocean and collectively known as Ligurian Units (Figure 1a; Conti et al., 2020 and references therein). Only a few ophiolite-bearing units preserve relics of HP-LT metamorphism, as in the Tuscan Archipelago (Gorgona and Giglio) and on the Argentario Promontory (Ricci & Serri, 1975; Theye et al., 1997; Jolivet et al., 1998b; Rossetti et al., 1999; 2001b). The Ligurian Units tectonically rest onto the anchimetamorphic continent-derived units of the Adria paleomargin (e.g., Carosi et al., 2003), consisting of Triassic–Paleogene passive margin sequences covered by Oligocene–Miocene foredeep deposits (Tuscan Nappe, Cervarola, and Umbria-Marche units in Figure 1a; Dallan Nardi & Nardi, 1972; Cerrina Feroni et al., 2002).

The metamorphic Tuscan-derived units, collectively known as the Tuscan Metamorphic Complex (TMC), crop out in the Northern Apennines hinterland at the base of the nappe stack, along the Tyrrhenian coast (Punta Bianca Promontory, Alpi Apuane, Monte Pisano, Mid Tuscan Ridge, Uccellina Mountains, Monte Argentario Promontory, Monti Romani) and in the Tuscan Archipelago (Elba and Giglio; Figure 1a). The TMC comprises a Paleozoic basement of phyllites, metavolcanics, and subordinate metalimestones, generally overlain by late Carboniferous–Triassic metasediments and in some areas by Triassic – Oligocene sequences analogue to the Tuscan Nappe. The late Carboniferous–Triassic sequence consists of phyllites, metasandstones, and the metasiliciclastic continental deposits of the Verrucano Group (quartzites, violet phyllites, and quartz-metaconglomerates), marking the beginning of the Alpine cycle (Rau & Tongiorgi, 1974; Lazzarotto et al., 2003; Aldinucci et al., 2008; Cassinis et al., 2018). The stratigraphic ages of the formation of the Paleozoic basement were largely constrained through correlations with similar sequences in Sardinia

and the Alps (e.g., Conti et al., 1991, 1993). However, the recent application of U-Pb detrital zircon geochronology allowed differentiation of Cambrian – Ordovician rocks of Gondwana affinity and late Carboniferous – Permian sequences representing the latest Variscan and earlier post-Variscan deposits (Musumeci et al., 2011; Paoli et al., 2017). Palynological data from the Paleozoic successions of southern Tuscany, recently yielded Carboniferous – Permian ages (Capezzuoli et al., 2021), suggesting that the occurrence of the pre-Carboniferous sequences could be restricted to northern Tuscany (Paoli et al., 2017) and the island of Elba (Musumeci et al., 2011) (Figure 1a).

The metamorphic evolution of the Paleozoic basement largely derives from garnet-bearing micaschists and gneisses drilled in the geothermal area of Larderello (Musumeci et al., 2002; Pandeli et al., 2005) and in the Pontremoli-1 well (Lo Pò et al., 2016), seldom exposed at surface (e.g. Cerreto pass; Molli et al., 2002; Franceschelli et al., 2004) (Figure 1a). In the Pontremoli 1 well, Lo Pò et al. (2016) documented Variscan (Upper Carboniferous – Permian) amphibolite-grade metamorphism (0.55 – 0.8 GPa and 520-575 °C). In the Monti Pisani, on the other hand, Paleozoic rocks show Alpine metamorphism recorded by chloritoid-bearing parageneses with a metamorphic climax at $T \sim 475$ °C and $P = 0.9 - 1.0$ GPa (Lo Pò & Braga, 2014).

At regional scale, the Alpine orogenic metamorphism (hereafter referred to as M_1) in the TMC is typified by HP/LT metamorphic gradients, equilibrated under greenschist- to blueschist-facies conditions (Franceschelli et al., 1986; Theye et al., 1997; Giorgetti et al., 1998; Jolivet et al., 1998b; Molli et al., 2000; Vignaroli et al., 2009; Bianco et al., 2015; Papeschi et al., 2020). In northern Tuscany (Figure 1a), the Verrucano Group yielded peak P–T conditions in the range of 0.5-0.9 GPa at 300 – 500 °C (Franceschelli et al., 1997; Jolivet et al., 1998b; Franceschelli & Memmi, 1999; Molli et al., 2000). The highest P/T paleogradients are recorded in southern Tuscany in the Mid-Tuscan Ridge (0.8 – 1.1 GPa at 350 – 420 °C);

Giorgetti et al., 1998; Brogi & Giorgetti, 2012), the Monte Argentario Promontory (0.8–1.0 GPa at 350–420 °C; Theye et al., 1997), and the island of Giglio (1.2 – 1.4 GPa at 310–350 °C; Rossetti et al., 1999). Metabasite-hosting metacarbonates from the island of Elba recorded up to 1.5–1.8 GPa at 320–370 °C (Papeschi et al., 2020). However, the age of the Alpine M₁ metamorphism remains poorly constrained. The ⁴⁰Ar/³⁹Ar geochronology on white mica provided variable ages for the metamorphic peak. The oldest, late Oligocene ages are from the Apuan Alps (26.5 – 27 Ma; Kligfield et al., 1986), where, however, the metamorphic age overlaps with the sedimentary protolith (Patacca et al., 2013), and Gorgona (25.5 ± 0.3 Ma; Rossetti et al., 2001b). Younger early Miocene ages, likely representing minimum ages, have been obtained on Elba (19.68 ± 0.15 Ma: Deino et al., 1992; 19.8 ± 1.4 Ma: Bianco et al., 2019; 20.99 ± 0.73 Ma: Ryan et al., 2021), the Uccellina Mountains (19.7 ± 0.4 Ma), and the Argentario Promontory (16.2 ± 0.3 Ma; Brunet et al., 2000).

The progressive rollback of the Adriatic subduction caused the diachronous opening of the Oligocene-Miocene Liguro-Provençal and the Neogene-Quaternary Tyrrhenian back arc basins (e.g., Malinverno & Ryan, 1986; Doglioni et al., 1999; Faccenna et al., 2001). Back arc-opening lead to widespread magmatism and associated high-temperature (HT) metamorphism in the region (Serri et al., 1993; Musumeci et al., 2002; Bertini et al., 2006; Rossetti et al., 2008; Papeschi et al., 2019), and the synchronous eastward propagation of thrust fronts towards the foreland (Patacca et al., 1990; Cosentino et al., 2010).

Early studies framed the exhumation of the HP units in the hinterland of the Apennine belt in a metamorphic core-complex style of post-orogenic extension (Carmignani & Kligfield, 1990; Carmignani et al., 1994). However, most of the studies favors syn-orogenic exhumation, based on the cold exhumation P–T paths (e.g. Jolivet et al., 1998b; Rossetti et al., 1999; Papeschi et al., 2020), occurrence of inverted metamorphic sequences (Jolivet et al.,

2008b; Molli et al., 2000; Carosi et al., 2004), and syn-compressional extensional faulting (Storti, 1995; Clemenzi et al., 2014; Massa et al., 2017; Ryan et al., 2021).

2.1 Geology of the Monti Romani

The Monti Romani area (Figure 1b) exposes a typical section of the Northern Apennine nappe edifice, formed by low-grade metamorphic rocks of the TMC, hereafter referred to as Monti Romani Complex (MRC), tectonically covered by discontinuous exposures of the Tuscan Nappe (TN) and Ligurian units (LU) (Azzaro et al., 1975). The MRC defines a NW-SE trending structural high, bounded by high-angle NNW-SSE striking extensional faults. These faults dissect the nappe pile and border grabens filled by Pliocene–Quaternary sedimentary and volcanic sequences (e.g., Varekamp, 1980; Moretti et al., 1990), including the Tafone Basin to the west (Figure 1b). The basin boundary fault systems control diffuse hydrothermal antimonite-bearing mineralization that was historically exploited (Dessau, 1951, 1952).

At the top of the nappe pile, the LU comprise several tectonic units representing fragments of Jurassic ophiolites and carbonatic-siliciclastic flysch deposits of Upper Cretaceous to Paleogene–Oligocene age (Dessau et al., 1972; Moretti et al., 1990; Figure 1b). Langhian–Serravallian deposits of the *Arenaria di Manciano* Fm cover the LU (Figure 1b; Martini et al., 1995; Bossio et al., 1998). The underlying TN (Figure 1b) shows a reduced stratigraphy in the area (*Serie Ridotta*; Signorini, 1949), with Oligocene–early Miocene foredeep deposits (*Macigno* and *Scaglia Toscana* Fms.) that directly overlie the late Triassic *Calcare Cavernoso* Fm., a carbonate evaporite that acted as detachment level during the nappe-stacking event (Burkhardt, 1947; Dessau et al., 1972; Moretti et al., 1990). The *Serie Ridotta* represents the result of tectonic elision of the Tuscan sequence, alternatively

interpreted as having occurred in an extensional (Lavecchia et al., 1984; Carmignani et al., 1994) or a compressional setting (Pertusati et al., 2004).

The MRC consists of a monotonous succession of graphitic phyllite and metasandstone, interlayered with rare lenses of metaconglomerate (Figure 1b). These rocks were first ascribed to the Triassic continental deposits of the Verrucano Group (Signorini, 1966; Alberti et al., 1970; Dessau et al., 1972), then tentatively correlated to the Carboniferous–Triassic (Cocozza et al., 1974; Azzaro et al., 1975), based on a correlation with the nearby Mt. Argentario (Mt. Argentario Sandstones; Decandia & Lazzarotto, 1980; Cirilli et al., 2002). Other authors correlated these rocks with the Cambrian–Silurian sequences cropping out in Tuscany and Sardinia (Moretti et al., 1990; Conti et al., 1991; Verrucchi et al., 1994). More recently, several Paleozoic units in the nearby Mid-Tuscan Ridge (Fig. 1a) were attributed to the Permian – Carboniferous post-Variscan sequences, based on the analysis of fossil palinological assemblages (Capezzuoli et al., 2021) and detrital zircon ages (Paoli et al., 2017). Although no geochronological and paleontological data exist for the MRC, a similar Carboniferous–Permian age is possible.

Regarding the metamorphic evolution of the MRC, early studies described greenschist-facies metamorphic conditions characterized by chlorite + white mica + quartz parageneses with accessory tourmaline, apatite, zircon, epidote, pyrite, and oxides (Dessau, 1951; Trigila, 1966; Dessau et al., 1972; Ricci, 1972). Azzaro & Di Sabatino (1974) first recognized the presence of paragonite and chloritoid in the area and suggested an Alpine origin for these metamorphic assemblages, referred to a Barrovian-type of metamorphism. They also determined the crystallinity of illite (Kubler, 1967), ascribing the MRC metamorphism to the low-grade type and suggesting Barrovian metamorphic conditions, with $T \sim 400\text{ }^{\circ}\text{C}$ and $P = 0.2\text{--}0.5\text{ GPa}$.

Early tectonic studies on the MRC highlighted the presence of NE verging folds, associated with a penetrative axial plane schistosity, later overprinted by NW-SE oriented extensional faults (Funiciello et al., 1984; Moretti et al., 1990; Conti et al., 1991). These authors documented a penetrative crenulation cleavage that, based on the inferred Paleozoic protolith age, they related to a polyphase (Variscan and Alpine) tectono-metamorphic evolution of the MRC (Funiciello et al., 1984; Moretti et al., 1990; Conti et al., 1991). However, some authors ascribed the metamorphism of the MRC only to the Alpine orogenic cycle (Ricci, 1972; Azzaro & Di Sabatino, 1974).

3. Materials and Methods

In order to define the tectono-metamorphic evolution of the Paleozoic rocks of the MRC, we carried out a comprehensive investigation of the area, involving a geological field survey (including structural analysis and sample collection), mineral analysis via electron microprobe (EMP) and powder X-ray diffraction (XRD), and whole rock chemistry via X-ray fluorescence (XRF). We utilised inverse (Raman spectroscopy of carbonaceous material (RSCM) and chlorite thermometry) and forward modelling phase equilibria modelling to elucidate the P-T conditions and metamorphic gradients experienced by the TMC.

A detailed description of the methods and analytical protocols is available in the Appendix. Table S1 shows the list of the investigated samples, their sampling coordinates, and mineral assemblage. We report the position of the samples also in Figure 1b and 2. Figures S1 and S2 show the analyzed RSCM spectra and related temperature estimates. The figures from S3 to S15 show the microstructural location of EMP mineral analyses. We provide XRD spectra in Figure S16 and S17, the Raman spectra of hematite in Figure S18, and rutile EDS spectra in Figure S19. The outputs of phase equilibrium modelling that are not shown in the main text are in Figure S20 to S23. We follow the mineral abbreviations by

Siivola & Schmid (2007). The original dataset is available in the repository associated with the present article at <http://dx.doi.org/10.17632/knrkh9cnnr4.3>

4. Structural analysis

The main tectonic fabric of the MRC is a penetrative S_p foliation (principal schistosity; Figure 3a, b). At map scale, the S_p ranges from subhorizontal to NNW–SSE striking and shows gentle to moderate (0–30°) NE- and SW-dip to the ENE and WSW, respectively, of the MRC, defining a regional-scale antiform, associated with minor open folds (Figure 2). Assuming a cylindrical shape of the regional fold, the β axis of this antiformal structure, derived from the dispersion of the poles to the S_p ($n = 146$) trends N345–03° (trend-plunge). The tectonic contacts with the anchimetamorphic TN and LU are sub-horizontal and follow the average attitude of the S_p foliation. However, at outcrop scale, high- and low-angle extensional faults, dominantly striking NNW–SSE, rework these first-order contacts.

At meso scale, S_p is defined by submillimetric sheets composed of oriented phyllosilicates and graphite, anastomosing around quartz-dominated layers, defining a slaty cleavage (*sensu* Passchier & Trouw, 2005). In most outcrops, the S_p foliation represents the only discernible mesoscale fabric (see below), which occurs as a continuous cleavage in phyllites and as a disjunctive cleavage in metasandstones (Figure 3a, b), respectively. Notably, S_p defines the axial surface of NE-verging, recumbent to overturned tight to isoclinal folds (F_p) and commonly fans close to fold hinges (Figure 3b). The primary lithological layering (bedding, S_0) is generally transposed and parallel to S_p . Locally, a small angle (< 15°) between S_p and S_0 can be observed across the metapelitic and metapsammitic layering (Figure 3a). Measured F_p fold axes are sub-parallel to the β -axis of the antiform,

defined by the S_p attitude at the map scale, trending N130-N170° ($n = 19$; average: N151°) with gentle (2–20°) plunge mostly towards the SSW (Figure 2).

In some localities, S_p is reworked by dm- to m-thick, top-to-the-NE ductile shear zones, defined by S-C tectonites and synthetic C' shear bands (Figure 3c, d). C- and C'-shear bands are associated with intensely foliated and lineated (SL) tectonites, showing well-developed quartz and phyllosilicate lineations (L_p ; Figure 3c). Measurements of associated S-foliations, C-shear bands and L_p stretching lineations are shown on the geological cross section in Figure 2. Shear zones frequently host cm-thick syntectonic quartz veins that are stretched parallel to shear bands (e.g., Figure 3d) or to the main S_p foliation (Figure 3c, e). These veins are boudinated as pinch-and-swell structures along NNW–SSE striking necks and refolded by tight to isoclinal recumbent folds (Figure 3e). Intensely deformed and veined outcrops typically show bands of light-colored phyllitic rocks displaying relatively coarse white mica and additional Mg-bearing minerals like chlorite or chloritoid, and lacking graphite (Figure 3c, d, e; see below).

Within the fine-grained domains, spaced crenulations, observable mostly at the microscale and rarely at the mesoscale, rework the S_p fabric. In general, the presence of crenulations is testified by tiny crenulation fold hinges, forming SSW–NNE trending intersection lineations (Figure 3f) on S_p , oriented sub-parallel to the L_p stretching lineations.

5. Petrography and microstructures

The dominant metamorphic assemblage of the MRC consists of a syn-tectonic assemblage made of quartz + K-white mica (muscovite) + rutile + Na-white mica (paragonite), graphite (hereafter referred to as graphite schists). A few samples lack graphite, and contain chlorite or chloritoid, and hematite as significant constituents (hereafter referred to as chloritoid schists and chlorite schist, respectively). Detrital white mica (with grains up

to 750 μm in size) is commonly present in the investigated lithologies. Zircon, apatite, and tourmaline constitute common accessory phases.

5.1 Graphite schists

Based on a visual estimate at thin section scale, in the graphite schists (samples R2, R14, R22a) quartz generally constitutes 50 – 70 % vol of the samples, while muscovite ranges 30–35 % up to 50 % vol and graphite 1–5 % vol (Figure 4a,b). Paragonite is not always present and constitutes less than 5 % vol, commonly occurring interlayered with muscovite (see below). Tiny amounts of rutile (less than 1 – 2 % vol) are present in all samples; remarkable is the lack of chlorite and albite in the main assemblage. Vermiculite is present as an alteration product after muscovite. Coarse, detrital muscovite grains are present in metapsammitic lithologies, where they form mica stacks surrounded by the metamorphic foliation (Figure 4b). Accessory minerals consist of syn-metamorphic apatite and rare tourmaline and zircon grains of detrital origin.

S_p is a continuous foliation defined by the preferred orientation of fine-grained (10–100 μm) muscovite, paragonite, rutile, and graphite grains and by the alternations of quartz- and mica-rich domains (Figure 4a, b). Quartz domains consist of coarser relic grains (100–500 μm), showing undulose extinction and surrounded by recrystallized equigranular (~ 30–50 μm sized) grains, with serrate to lobate boundaries associated with tiny bulges. A discrete crenulation cleavage, with a spacing of some hundreds of micrometers, locally refolds the S_p mineral fabric (Figure 4c).

5.2 Chlorite schist

The mineral assemblage of chlorite schists (sample R15b; Figure 4d-f) consists of muscovite (40–50 % vol), chlorite (30 – 35 % vol), quartz (15–20 % vol), paragonite (< 5 %

vol), hematite (1 – 2 % vol), and rutile (1–2 % vol). Quartz-rich layers locally contain calcite grains (Figure 4e), and some detrital tourmaline grains occur.

This sample shows a tightly crenulated continuous S_p foliation, defined by the preferred orientation of fine-grained chlorite, muscovite, paragonite, quartz, and hematite grains (Figure 4d, f). The crenulation cleavage shows a spacing of 100 – 200 μm , with crenulation cleavage planes defined by re-oriented muscovite, paragonite, quartz, and hematite.

5.3 Chloritoid schists

The chloritoid schists (Figure 5; samples R6, R17) consist of quartz (60–50 % vol), muscovite (25–30 % vol), chloritoid (5–10 % vol) associated with minor hematite (1–5 % vol) and rutile (< 1 % vol). Paragonite is present as an accessory only in sample R6. Hematite is volumetrically significant in sample R17, and present in trace amounts in sample R6. Kaolinite is also present as an alteration product after chloritoid. These samples show a single, continuous S_p slaty cleavage, defined by the orientation of muscovite grains (Figure 5a). The foliation envelopes irregular quartz lenses, with a thickness of 100–200 μm , showing similar fabric compared to the graphite schists. Chloritoid grains show a grain size of 50–150 μm (long axis) and subhedral to euhedral habit (Figure 5b-c). They are generally oriented along the S_p (Figure 5d), although many grains appear oriented at random angles with cleavage planes, indicating syn- to post-kinematic growth with respect to the muscovite-defined S_p (Figure 5b-c). Significantly, we did not observe detrital mica grains in the chloritoid schists.

6. Mineral chemistry

We acquired EMP chemical analyses of the constituent minerals (Figures S3 to S15) from representative samples of graphite (R2, R14, and R22b), chlorite (R15b), and chloritoid (R6, R17) schists. We calculated the Fe^{3+} content of chloritoid on a stoichiometric basis. We show representative mineral analyses in Table 1 and 2. In the following text, we describe mineral compositions in terms of $X_{\text{Fe}} = [\text{Fe}/(\text{Mg} + \text{Fe}^{\text{total}})]$, $X_{\text{Mg}} = [\text{Mg}/(\text{Mg} + \text{Fe}^{\text{total}})]$, with Fe representing the total iron, and $X_{\text{Na}} = [\text{Na}/(\text{K} + \text{Na})]$ (molar proportions).

6.1 Graphite schists

In the investigated samples of graphite schists, white micas show negligible Mn content and $\text{Ti} = 0.00\text{--}0.03$ cations per formula unit (pfu) (Table 1). Ca is present in traces (<0.02 pfu), whereas Ba is within $0.08\text{--}0.20$ wt%, with some analyses showing up to 0.44 pfu (Table 1). In the $\text{Al}^{\text{VI}}\text{--Si}$ pfu plot, K-white mica compositions cluster close to the muscovite endmember, with Si ranging from 3.05 to 3.20 pfu and Al^{VI} ranging $1.76\text{--}2.00$ pfu, with few outliers up to 3.34 Si pfu and down to $1.58\text{--}1.60$ Al^{VI} pfu (Figure 6a). The $[\text{Mg} + \text{Fe}^{\text{total}}]\text{--Si}$ pfu plot shows that muscovite has variable contents of $[\text{Mg} + \text{Fe}^{\text{total}}]$, between $0.02\text{--}0.44$ pfu (Figure 6b), indicating the presence of micas with metamorphic and detrital origin. The composition trends towards the celadonite component, indicating the presence of Fe^{3+} (Figure 6b). The X_{Fe} of muscovite and paragonite largely lies within 0.34 and 0.54 , with outliers spanning from 0.24 to 0.64 (Figure 6c). The proportion of the paragonite endmember (X_{Na}) in muscovite is dominantly between 0.04 and 0.22 (Figure 6c). As analyses with $X_{\text{Na}} = 0.2\text{--}0.7$ are in the range of the muscovite–paragonite solvus (e.g., Guidotti, et al., 1994), we interpret analyses that lie in this range (Figure 6c) as fine-grained metamorphic mixtures of the two micas.

6.2 Chlorite schist (R15b)

The K-white mica compositions (Table 1) lie in the Al^{VI} -Si pfu plot close to the muscovite endmember, showing Si = 3.04–3.10 pfu and Al^{VI} = 1.78–1.86 pfu (Figure 6d). Ti, Mn, Ca, and Ba are present as trace elements < 0.01–0.04 pfu (Table 1). The $[\text{Mg} + \text{Fe}^{\text{total}}]$ varies between 0.16 and 0.39 pfu (Figure 6e). Deviations from the ideal Tschermak substitution indicates the presence of Fe^{3+} and, possibly, analyses that are mixed with chlorite, which is commonly finely interlayered with muscovite in the sample. Paragonite is also finely interlayered with muscovite and we obtained only mixed analyses of this mineral (Figure 6f). Muscovite analyses show $X_{\text{Na}} = 0.02\text{--}0.20$ (largely below 0.05) and $X_{\text{Fe}} = 0.58\text{--}0.78$ (Figure 6f).

Chlorite shows Si = 2.51–2.61 and very restricted $X_{\text{Mg}} = 0.66\text{--}0.68$ (Figure 6g). Ti in chlorite is between 0.02–0.04 pfu, while Mn is in the 0.04 – 0.11 pfu range (Table 2). Recalculated chlorite compositions, based on the Vidal & Parra (2000) endmember scheme, show that the analyses can be expressed as 0.37–0.40% of clinocllore, 0.19–0.20% of daphnite, 0.39–0.44% of amesite. Some octahedral totals sum above 6.00, thus indicating the presence of minor Fe^{3+} in the formula. A normalization to cation sum = 10 and 14 oxygens results in $\text{Fe}^{3+} = 0.00\text{--}0.16$ pfu.

In order to derive temperature estimates from the available chlorite analyses, we applied four different empirical chlorite geothermometers (Table 2). Based on the application of the Cathelineau (1988), Jowett (1991), and Xie et al. (1997) geothermometers, we obtained an average temperature estimate of 398 ± 8 °C on 11 analyses. Application of the Kranidiotis & MacLean (1987) geothermometer yielded a lower temperature estimate of 346 ± 5 °C (Table 2). This lower estimate is likely a result of the lower calibration temperature of this geothermometer ($T < 300$ °C).

6.3 Chloritoid schists (R6 and R17)

The composition of K-white mica in the chloritoid schists is slightly more scattered in sample R6 and more clustered in sample R17, being in both cases close to the muscovite endmember (Figure 6d, e). In R6, muscovite shows $\text{Si} = 3.04\text{--}3.26$ pfu, $\text{Al}^{\text{VI}} = 1.72\text{--}1.99$ pfu, $[\text{Mg} + \text{Fe}^{\text{total}}] = 0.16\text{--}0.31$ pfu, and X_{Fe} largely between 0.60 and 0.76, with outliers down to 0.30 (Figure 6d, e, f). In R17, muscovite has $\text{Si} = 3.0\text{--}3.10$ pfu, $\text{Al}^{\text{VI}} = 1.85\text{--}1.88$ pfu, $[\text{Mg} + \text{Fe}^{\text{total}}] = 0.17\text{--}0.20$, and $X_{\text{Fe}} = 0.63\text{--}0.73$ (Figure 6d, e, f). Both samples show muscovite analyses clustered at $X_{\text{Na}} = 0.11\text{--}0.20$, with no mixed muscovite-paragonite analyses, and a single paragonite analysis in sample R6 with $X_{\text{Na}} = 0.89$ (Figure 6f). Mn, Ti, Ca, and Ba are present in traces $< 0.01\text{--}0.02$ pfu (Table 1).

Both samples show chloritoid with $\text{Ti} < 0.01$ and $\text{Mn} = 0.01\text{--}0.03$ pfu, with a core-to-rim Fe-Mg-zoning (Figure 6h, 7; Table 2). In sample R6, chloritoid composition is relatively homogeneous, with $\text{Fe}^{2+} = 1.63\text{--}1.76$ pfu, $\text{Fe}^{3+} = 0.05\text{--}0.29$ pfu, and $\text{Mg} = 0.19\text{--}0.30$ pfu (Table 2). Moving from core to rim, the X_{Mg} ratio varies from 0.09–0.13 to 0.13–0.14, respectively (Figure 6h, 7a-b). In sample R17, the compositional variability is larger, with $\text{Fe}^{2+} = 1.33\text{--}1.71$, $\text{Fe}^{3+} = 0.00\text{--}0.27$ pfu, and $\text{Mg} = 0.23\text{--}0.56$ pfu, with extensive core to rim zoning preserved in larger chloritoid grains (Figure 6h, 7c-f). In general cores, show $X_{\text{Mg}} = 0.11\text{--}0.15$, while rims reach $X_{\text{Mg}} = 0.23\text{--}0.27$ (Figure 6f, 7e-f).

7. RSCM thermometry

We obtained Raman spectra on seventeen samples, geographically distributed across the MRC (Figure 2 and Table 4). Representative spectra are shown in Figure 8 (all spectra are available in Figure S1 and S2). RSCM results indicate that the spectra are remarkably similar throughout the whole MRC (Table 4; Figure 8), and comparable to those typical of greenschist-facies domains (e.g., Rahl et al., 2005).

Collectively, the Raman spectra of MRC samples exhibit two main defect bands, a D2 band located around 1620 cm^{-1} , and a wider and more intense D1 band around 1350 cm^{-1} (Figure 8). Samples show a narrow, constant G band, located between 1575 and 1590 cm^{-1} . The variability in G band position can be appreciated only by comparing different samples, indicating it most likely reflects original CM characteristics. Band-areas were used to calculate the Raman parameter R2, which varies between 0.54 and 0.60 (Table 3). Intra-sample carbonaceous material homogeneity is indicated by low values of standard deviation for the parameter R2, always below 0.06 (Table 3). The overall data set shows limited difference in peak temperatures throughout the MRC, with values ranging between 367 and $401\text{ }^{\circ}\text{C}$ (Figure 2) and standard deviations between 6 and 13°C (Table 3). The mean metamorphic temperature across the MRC is $382 \pm 8\text{ }^{\circ}\text{C}$. The small variation range of Raman temperatures and the absence of clear temperature gradients in the MRC (Figure 2), indicate that the peak metamorphic temperatures in the MRC were highly homogeneous.

8. Phase equilibria modelling

For phase equilibria (pseudosection) modelling, we recalculated the bulk composition of the samples (shown as wt% in Table 4) into the $\text{MnO-Na}_2\text{O-CaO-K}_2\text{O-FeO-MgO-Al}_2\text{O}_3\text{-SiO}_2\text{-H}_2\text{O-TiO}_2\text{-O}_2$ (MnNCKFMASHTO) system. We fractionated P_2O_5 as apatite, together with corresponding amounts of CaO, in order to correct CaO for the presence of phosphates that we did not model. This recalculation eliminated CaO entirely from all samples except for the chlorite schist (R15b), where CaO is chiefly stored in carbonate. We, therefore, excluded CaO, P_2O_5 , and CO_2 from the calculation, considering apatite and calcite as excess phases.

We performed pseudosection modelling using PERPLE_X 6.8.6 (Connolly, 2005, 2009) and the hp02ver.dat thermodynamic dataset (Holland & Powell, 2001; Connolly &

Kerrick, 2002). We considered quartz, lawsonite, rutile, and titanite as pure phases. The adopted solution models were: Gt(W) – garnet, St(W) – staurolite, Ctd(W) – chloritoid, Mica(W) – white mica, Chl(W) – chlorite, Bi(HGP) – biotite (White et al., 2014), cAmph(DP) – clinoamphibole (Diener & Powell, 2012), Ep(HP) – epidote (Holland & Powell, 1998), Omph (GHP) – clinopyroxene (Green, Holland, & Powell, 2007), Stlp(M) – stilpnomelane (Massonne, 2010), MtUl(A) – magnetite (Andersen & Lindsley, 1988), feldspar – ternary feldspar (Fuhrman & Lindsley, 1988), and the ideal IlGkPy – ilmenite, Carp – carpholite, hCrd – cordierite, and T – talc models. We chose these models, specifically the ‘(W) models’ by White et al. (2014) to model Fe^{3+} in our samples. However, since many of these models do not include Mn, we also calculated alternative pseudosections with the Gt(HP) – garnet, St(HP) – staurolite, Ctd(HP) – chloritoid, Pheng(HP) – K-white mica, Omph(HP) – clinopyroxene, Chl(HP) – chlorite (Holland & Powell, 1998), Bio(TCC) – biotite (Tajčmanová et al., 2009), Mica(M) – Na-white mica, and Namph(M) – Na-amphibole (Kryza et al., 2011) models (Figure S21, S22, S23).

We modelled chlorite and chloritoid schists considering the fluid phase as pure H_2O , whereas we used the COH hybrid equation of state by Connolly & Cesare (1993), with H_2O content in the fluid phase buffered by presence of graphite. Since the Ctd(W) model does not incorporate Mn in chloritoid, its use on our chlorite-free samples results in a dramatic expansion of the Mn-rich carpholite- and garnet-bearing fields towards lower greenschist-facies conditions. To overcome this problem, we did not consider Mn (0.01–0.02 wt% MnO , close to detection limit) in the calculation of phase equilibria for the chloritoid schists R6 and R17. In any case, we noted that with such tiny Mn contents the stability fields do not change substantially when using the Ctd(HP) model, which considers Mn in the solid solution (Figure S22, S23). Therefore, we consider the effect of the analyzed small bulk-rock Mn contents on the calculated paragenesis to be negligible.

In the $[\text{Mg} + \text{Fe}^{\text{total}}]$ pfu–Si pfu diagram, all samples show white mica analyses corresponding to muscovite compositions that deviate from the ideal Tschermak trend (Figure 6b, e), indicating the presence of Fe^{3+} in the mineral. Moreover, the chlorite (R15b) and chloritoid schists (R6 and R17) contain hematite as a primary constituent, which requires elevated oxygen fugacity. In order to estimate the amount of ferric iron in the chlorite and chloritoid schists, we calculated preliminary P–T pseudosections considering all iron as divalent, fluid (H_2O) in excess, and a P–T range of 0.2–2.0 GPa and 300–600 °C. Subsequently, we calculated P– $X_{\text{Fe}_2\text{O}_3}$ ($= [\text{Fe}^{3+}/(\text{Fe}^{2+} + \text{Fe}^{3+})]$; e.g. Lopez-Carmona et al., 2013; Lo Pò & Braga, 2014) pseudosections between $P = 0.2\text{--}2.0$ GPa and $X = 0\text{--}1$, for T at 340, 380, and 420 °C (representing the average and the extremes of the T estimated via RSCM thermometry, respectively).

We show the most relevant pseudosections ($T = 380$ °C for the chlorite schist R15b and the chloritoid schists R6 and R17; $T = 420$ °C for the chloritoid schist R17). We used P– X pseudosections to estimate the proper $X_{\text{Fe}_2\text{O}_3}$ ratio that best fits with the observed parageneses and mineral chemistry. Finally, we calculated P–T pseudosections for each sample, based on the $X_{\text{Fe}_2\text{O}_3}$ values estimated on P– X pseudosections. We discuss the results of modelling in the next sections.

8.1 Graphite schists

The graphite schists all show the same metamorphic assemblage (quartz + muscovite + paragonite + graphite + rutile) and provide little scope to derive P–T constraints through pseudosection modelling. An example is shown in Figure S20 in the supplementary material. The field that best approximates the observed parageneses is the chlorite + muscovite + paragonite + chloritoid + quartz + rutile field, stable for $T < 460$ °C and $P = 0.2\text{--}1.5$ GPa (Figure S20). The Si pfu content of muscovite in the graphite schist R22b (3.04 – 3.19

excluding outliers; Figure 6a) further constrains the peak pressure to 1.0–1.2 GPa. However, this should be considered as a rough estimate, since we observed neither chlorite nor chloritoid, predicted by the calculation. We calculated the mode of chloritoid expected in the chlorite + muscovite + paragonite + chloritoid + quartz + rutile field, which ranges 1–2% vol in the 1.0–1.2 GPa pressure interval (Figure S20). The total amount of Mg and Fe in wt% expected in muscovite by the pseudosection is 1.5–2.5 wt% at 1.0–1.2 GPa. Nevertheless, the analyzed muscovite grains contain up to 5 wt% of $[\text{Mg} + \text{Fe}^{\text{total}}]$ (corresponding to 0.23–0.40 $[\text{Mg} + \text{Fe}^{\text{total}}]$ pfu; Figure 6b and Table 1). This misfit may explain the lack of chloritoid and/or chlorite in these samples.

8.2 Chlorite schist (R15b)

The chlorite schist contains the syn-metamorphic assemblage quartz + chlorite + muscovite + paragonite + rutile + hematite. The calculated P–T diagram for $X_{\text{Fe}_2\text{O}_3} = 0$ is characterized by many fields that show three to four coexisting phyllosilicate phases (muscovite, paragonite, chlorite, and biotite; Figure 9). Muscovite and quartz are stable across the entire P–T range, whereas rutile is present in all fields except for those calculated at $T = 460\text{--}540\text{ }^\circ\text{C}$ at low P (Figure 9). Paragonite is the dominant Na-bearing phase, except at $P > 1.7\text{--}1.8\text{ GPa}$, where it is replaced by either jadeite or glaucophane, and for $P < 0.6\text{--}0.7\text{ GPa}$ where it coexists with or is replaced by albite (at $300\text{--}420\text{ }^\circ\text{C}$) and muscovite ($T > 420\text{ }^\circ\text{C}$) with Na-rich composition (Na-rich muscovite). Biotite is steadily present at higher temperature conditions ($P < 1.2\text{--}1.6\text{ GPa}$; $T > 420\text{ }^\circ\text{C}$), while garnet is ubiquitous at $P > 0.6\text{ GPa}$ and $T > 480\text{--}500\text{ }^\circ\text{C}$ (Figure 9).

The chlorite + muscovite + paragonite + quartz + rutile paragenesis observed in the sample (except for hematite) is stable at $P = 0.6\text{--}1.4\text{ GPa}$ and $T = 300\text{--}500\text{ }^\circ\text{C}$ in a large high-variance field, delimited towards lower pressures by the presence of albite- and/or biotite-

bearing fields and towards higher pressures by carpholite- and/or chloritoid-bearing fields (Figure 9). Within this field, muscovite shows Si isopleths between 3.20–3.24 pfu and $X_{\text{Fe}} = \sim 0.40 - 0.50$. These values are higher in Si and lower in X_{Fe} than the observed muscovite composition (Figure 6d, f). Moreover, the modelled X_{Mg} of chlorite is around 0.41–0.46, while its observed composition is steadily around 0.66–0.68 (Figure 6g).

In the P– $X_{\text{Fe}_2\text{O}_3}$ diagram, the addition of Fe^{3+} causes the appearance of hematite in all fields and stabilizes the chlorite + muscovite + paragonite + quartz + rutile + hematite paragenesis towards lower pressures at increasing $X_{\text{Fe}_2\text{O}_3}$ (Figure 10a). We observe a similar change in carpholite-bearing fields, stabilized towards lower pressures, and albite-bearing fields, confined to even lower pressures with increasing Fe^{3+} content. Chloritoid is entirely absent for $X_{\text{Fe}_2\text{O}_3} > 0.2$. Within the chlorite + muscovite + paragonite + quartz + rutile + hematite field, we noticed a correspondence between the observed mineral chemistry and the calculated compositional isopleths. Indeed, for $X_{\text{Fe}_2\text{O}_3} = 0.6$ –0.8, chlorite shows X_{Mg} of 0.64 – 0.68 and Si isopleths of muscovite range at 3.05 – 3.10 pfu, consisted with the observed muscovite and chlorite chemistry (Figure 6d, g). The best fit occurs at $X_{\text{Fe}_2\text{O}_3} \sim 0.6$ (Figure 10a). At these conditions, however, the modal content of hematite is about 3 % vol, higher than observed (1–2 % vol), and the X_{Fe} in muscovite is lower, around 0.30. The higher modal content of hematite could be a combined effect of its modal underestimation and the choice of solution models, which may underestimate the ferric component in Fe, Mg-bearing phases. For example, the calculated muscovite generally shows less $[\text{Mg} + \text{Fe}^{\text{total}}]$ pfu than observed. This may also affect the calculated X_{Fe} for muscovite, especially at high $X_{\text{Fe}_2\text{O}_3}$ values.

In Figure 10b we show the P-T pseudosection calculated using $X_{\text{Fe}_2\text{O}_3} = 0.6$. The chlorite + muscovite + paragonite + quartz + rutile + hematite field is now stable at a lower P-T range, between 0.3 – 1.2 GPa and 300–500 °C. In this field, muscovite shows Si

isopleths ranging 3.08–3.10 pfu and chlorite shows $X_{Mg} \sim 0.66$. Using RSCM results, we can restrict this range to $P = 0.4\text{--}1.2$ GPa and $T = 340\text{--}420$ °C.

8.3 Chloritoid Schist (R6)

Sample R6 consists of the muscovite + chloritoid + quartz + rutile + hematite assemblage associated with rare paragonite. Notably, neither chlorite nor pyrophyllite/kyanite were observed. For $X_{Fe_2O_3} = 0$, quartz and muscovite are stable in all fields, chloritoid and rutile are ubiquitous for $T < 500\text{--}580$ °C (Figure 11). Fields in the HP-LT corner of the diagram ($P > 0.9\text{--}1.0$ GPa at $T < 420\text{--}440$ °C) contain carpholite and/or paragonite. In the same pressure range but at higher T ($> 460\text{--}540$ °C), chloritoid coexists with either kyanite or staurolite, while garnet occurs in the chloritoid-absent fields. At low $P < 0.8\text{--}0.9$ GPa, chlorite and/or ilmenite become modally important. The muscovite + chloritoid + quartz + rutile paragenesis defines a large P-T field comprised between $P = 0.7\text{--}1.8$ GPa and $T = 395\text{--}560$ °C, bordered at low pressure by chlorite-bearing fields and at high P by carpholite-, kyanite- and staurolite-bearing fields, respectively (Figure 11). The calculated X_{Mg} isopleths of chloritoid show lower values in this field (0.11–0.12), which fit with the X_{Mg} values observed in the chloritoid core but not with those observed in the rim (up to $X_{Mg} = 0.13\text{--}0.14$; Figure 6h). Analyzed muscovite compositions, with Si largely between 3.05–3.15 pfu excluding outliers (Figure 6d), are fully consistent with the Si isopleths calculated for this field ($\sim 3.06\text{--}3.07$ pfu). Calculated muscovite X_{Fe} ratios (observed values: 0.65–0.70) intersect with the Si isopleths only in the carpholite-bearing fields for $P \sim 1.6\text{--}1.8$ GPa at $T < 360$ °C.

In the $P\text{--}X_{Fe_2O_3}$ diagram (Figure 12a), a slight increase of $X_{Fe_2O_3}$ to 0.10–0.15 decreases the stability range of chlorite, which is not present for $T = 380$ °C at $X_{Fe_2O_3} > 0.15$. At such enhanced $X_{Fe_2O_3}$, the presence of an Al-bearing phase, like pyrophyllite, is

predicted, as the ratio $Al/(Fe^{2+} + Mg)$ of the rock is getting higher accordingly. The muscovite + chloritoid + quartz + rutile + hematite paragenesis is stable in a very restricted range at $T = 380\text{ }^{\circ}\text{C}$, between 0.2–0.7 GPa and 0.10–0.15 $X_{Fe_2O_3}$ (Figure 12a). Consistent with its analyzed composition (Figure 6h), within this field we observe X_{Mg} values of 0.13–0.14 for chloritoid. However, the calculated Si isopleths of muscovite (3.02–3.03 pfu) are lower compared to the observed composition (Figure 6d). The X_{Fe} of muscovite in this field is about 0.3, lower than observed (Figure 6f).

Overall, the $X_{Fe_2O_3}$ value of 0.1 represents the best fit for reproducing the observed metamorphic assemblage, and the muscovite and chloritoid compositions. Therefore, we calculated a P-T diagram for $X_{Fe_2O_3} = 0.1$ (Figure 12b). The muscovite + chloritoid + quartz + rutile field, now containing also hematite, occurs at $P = 0.45\text{--}1.25$ GPa for $T = 375\text{--}500\text{ }^{\circ}\text{C}$ (Figure 12b). With respect to the Fe^{3+} - free case, carpholite, paragonite, or kyanite occur at higher pressures, whereas chlorite and magnetite are present at lower pressures. X_{Mg} of chloritoid is constantly around 0.14 in this field, while the Si isopleths of muscovite range between 3.02 and 3.03 pfu. The X_{Fe} of muscovite is around 0.25 – 0.45. Based on the maximum T estimated through the RSCM thermometry, the stability of the observed metamorphic assemblage can be restricted to $P = 0.6\text{--}1.1$ GPa and $T = 375\text{--}420\text{ }^{\circ}\text{C}$ (Figure 12b).

8.4 Chloritoid Schist (R17)

Sample R17 consists of the assemblage muscovite + chloritoid + quartz + rutile + hematite. The calculated P-T diagram for $X_{Fe_2O_3} = 0$ shows the widespread presence of coexisting chloritoid and chlorite or paragonite in all fields for $T < 500\text{--}560\text{ }^{\circ}\text{C}$ (Figure 13). Quartz and muscovite are present in all fields, whilst rutile is stable for $T < 460\text{--}540\text{ }^{\circ}\text{C}$. At higher T ($> 460\text{--}500\text{ }^{\circ}\text{C}$) most fields contain garnet, ilmenite, and biotite, whereas carpholite

is an important rock-forming phase for $P > 1.0$ GPa at low T (300 – 400 °C). The chlorite-absent muscovite + chloritoid + quartz + rutile pentavariant field occurs over a restricted range for high pressures (> 1.3 GPa) at $T = 490–40$ °C, well above of the RSCM estimates (Figure 13). In this field, calculated muscovite Si isopleths are higher (> 3.18 pfu) than those observed (3.05–3.10 pfu; Figure 6d). The analyzed muscovite compositions are stable at $T \sim 400–440$ °C and $P = 0.7–1.0$ GPa in the muscovite + chlorite + chloritoid + quartz + rutile field (Figure 13). The calculated X_{Mg} of chloritoid is in the range of 0.01 – 0.12 (Figure 13), reaching a maximum of 0.08 in the muscovite-paragonite-chloritoid-quartz-rutile and chlorite-muscovite-chloritoid-quartz-rutile fields. Higher X_{Mg} values are reached in the presence of biotite and/or garnet at higher temperatures, well beyond the 360–400 °C temperature range estimated with RSCM thermometry. Overall, the observed parageneses are not consistent with the metamorphic assemblage of the chloritoid schist R17, with the analyzed chloritoid composition, being $X_{Mg} = 0.13–0.28$ (Figure 6h).

Figure 14 shows that addition of Fe^{3+} to the bulk composition has a dramatic effect on the stability of chlorite, which, for $P < 1.0$ GPa, disappears for $X_{Fe_2O_3} \sim 0.30–0.35$ at $T = 380–420$ °C. The muscovite-chloritoid-quartz-rutile-hematite field, corresponding to the assemblage observed in the sample, appears for a minimum value of $X_{Fe_2O_3} = 0.37–0.40$ and $P < 0.6$ GPa at 380 °C (Figure 14a) and expands at 420 °C to $P = 0.2–1.4$ GPa and $X_{Fe_2O_3} = 0.2–0.4$ (Figure 14b). The chloritoid core composition is reproduced in this field at 420 °C (calculated $X_{Mg} = 0.13–0.17$; observed $X_{Mg} = 0.11–0.17$; Figure 6h), corresponding to Si in muscovite below 3.05 pfu. Although the muscovite-chloritoid-quartz-rutile-hematite field is limited at T of ~ 380 °C, the observed muscovite (Si pfu) and chloritoid (X_{Mg}) compositions intersect for $X_{Fe_2O_3} = 0.3–0.4$ and $P < 0.7–0.8$ GPa. However, the calculated X_{Fe} of muscovite (~ 0.30) is not consistent with the observed mineral chemistry (Figure 6f; Table 1).

A P-T pseudosection calculated for $X_{\text{Fe}_2\text{O}_3} = 0.3$ is shown in Figure 15. This pseudosection contains a wide field with muscovite + chloritoid + quartz + rutile + hematite, comprised between 0.5 – 1.6 GPa and 390–520 °C, which is bounded by magnetite- and chlorite-bearing fields towards lower pressures ($< 0.5 - 0.7$ GPa) and carpholite- ($T < 440$ °C) or kyanite-fields ($T > 440$ °C) at higher pressures (0.8 – 1.6 GPa), respectively. Within the muscovite-chloritoid-quartz-rutile-hematite field, muscovite shows Si isopleths of ~ 3.05 pfu and chloritoid X_{Mg} of ~ 0.14 , consistent with the measured compositions of the muscovite and the chloritoid cores (Figure 6d-h). However, the predicted X_{Fe} of muscovite is in the range 0.25–0.45, lower than observed (0.63–0.73; Figure 6f). The RSCM thermometry results allows to further constrain the P-T stability of the observed metamorphic assemblage to 0.7–1.2 GPa and 380–420 °C (yellow field in Figure 15). These P-T estimates are based on the composition of the chloritoid core, since modelling did not reproduce the observed chloritoid rim compositions (up to $X_{\text{Mg}} = 0.27$; Figure 6h) in equilibrium with the observed assemblage. Two possible mechanisms that could explain such an extreme zoning are discussed in section 9.3.

9. Discussion

The structure and metamorphic evolution of the MRC has remained largely unconstrained for decades. Early studies focused primarily on the lithostratigraphic features of the area and only a few of them attempted a structural reconstruction. These studies proposed that the tectono-metamorphic evolution of the MRC was polyphase, due to a combination of Variscan and Alpine deformation events (Funicello et al., 1984; Moretti et al., 1990; Conti et al., 1991).

9.1 Metamorphic conditions

Chloritoid- and chlorite-bearing assemblages represent the exception rather than the rule in the MRC and are present only in 3 out of the 50 samples collected in the present study (Table S1). Most samples from the MRC contain the assemblage muscovite + paragonite + quartz + rutile + graphite. The RSCM thermometry results on the graphite-bearing samples are roughly constant across the MRC and constrains the upper temperature limit of metamorphism to ~ 340–420 °C (considering errors; Table 4), indicating a quite homogeneous peak thermal structure, and suggesting no differential exhumation within the MRC. The chlorite geothermometry yielded temperatures between 390 – 410 °C (Table 2), providing an independent temperature estimate on a sample lacking graphite, which is consistent with the temperature estimates obtained via RSCM.

Thermodynamic modelling applying complex solid solution models can be considered as tentative at low-T conditions. Nonetheless, the modelled chlorite- and chloritoid-bearing samples indicate consistent metamorphic P-T conditions of 0.4–1.2 GPa at 340–420 °C for the chlorite schists (sample R15b) and 0.6–1.2 GPa at 380–420 °C for chloritoid schists (samples R6 and R17), respectively. The combination of RSCM and chlorite geothermometry with the Si pfu isopleths of syn-metamorphic muscovite allows the P-T stability of the chlorite- and chloritoid-bearing parageneses to be restricted to a narrower thermo-baric field when compared to the larger P-T ranges calculated via phase equilibria modelling. Therefore, although the forward modelling fails in reproducing the metamorphic assemblage of the graphite-bearing samples, these P-T estimates converge at $P = 0.7 - 1.1$ GPa and $T = 380 - 420$ °C, a HP/LT thermo-baric environment that we consider as representative of the peak metamorphic conditions reached by the MRC.

9.2 Structural evolution

The presented structural, microstructural, and metamorphic data show that the MRC preserves a principal plano-linear deformation fabric (S_p - L_p), which transposes the primary fabric (S_0) during blastesis of HP-LT chloritoid-, chlorite-, muscovite/paragonite-bearing assemblages (Figure 3 to 7). Stretching lineations trend roughly SW – NE and are associated with overall top-to-the-NE sense of shear, consistently with typical Alpine orogenic trends/vergence found in the exhumed metamorphic complexes in the hinterland of the Northern Apennines (e.g., Carmignani & Kligfield, 1990; Keller & Coward, 1996; Jolivet et al., 1998b; Molli et al., 2000; Molli & Vaselli, 2006). Tectonic foliations across the MRC, ranging from subhorizontal to gently NE and SW dipping, define an antiformal structure, which is common in other exposures of the TMC (e.g., Carmignani & Kligfield, 1990; Carmignani et al., 1994; Molli & Vaselli, 2006; Papeschi et al., 2017). The observed HP-LT chloritoid-bearing parageneses are compatible with similar Alpine assemblages that have been described in nearby TMC exposures, e.g., in the Argentario (Theye et al., 1997), and the Mid-Tuscan Ridge (Giorgetti et al., 1998; Brogi and Giorgetti, 2012; Giuntoli & Viola, 2021) (Figure 1a). The RSCM thermometry (average peak T of 382 ± 8 °C) does not support a Variscan tectono-metamorphic inheritance within the MRC, since its thermal structure is not compatible with the hotter environments (HT greenschist- to amphibolite-facies conditions) documented for the Variscan metamorphism in the region (e.g., Franceschelli et al., 2004; Pandeli et al., 2005; Lo Pò et al., 2016).

We therefore propose that the development of the composite S_p - L_p fabric and the syn-kinematic blastesis of quartz + muscovite + paragonite + rutile + graphite \pm chlorite \pm chloritoid \pm hematite was invariably linked to an Alpine deformation event and does not preserve relics of a previous Variscan history. We thus interpret the tectono-metamorphic fabric described in this study as corresponding to S_1 - L_1 tectonites, produced during a

progressive D₁ deformation event that we correlate at regional scale with the D₁/M₁ Alpine orogenic phase of the TMC, linked to construction of the Apennine chain (e.g., Carmignani & Kligfield, 1990; Jolivet et al., 1998b; Molli et al., 2000; Molli & Vaselli, 2006; Papeschi et al., 2020). Within this scenario, crenulations (and the associated intersection lineations L_c) in the MRC phyllites can be explained as local, composite fabrics (*sensu* Tobisch & Patterson, 1988), related either to progressive deformation or strain partitioning during the progress of the D₁/M₁ event within the strongly foliated rocks that make up the MRC.

9.3 Origin of chloritoid zoning

The investigated chloritoid schists show extensive chloritoid X_{Mg} core to rim zoning, spanning from 0.13 to 0.27 in sample R17. As documented by thermodynamic modelling of the MRC samples, a change in P-T conditions at isochemical conditions cannot explain such a wide range of chloritoid compositions. Furthermore, RSCM thermometry indicates an uniform thermal structure (with maximum T of ~ 400–420 °C) across the MRC, ruling out the possibility that the chloritoid zoning could have been produced by a temperature increase. In addition, the scattered vs. clustered muscovite compositions documented in the graphite and chloritoid samples, respectively (Figure 6a, b, d, e), together with the almost complete transposition of the early textural fabric in the chloritoid samples (Figs. 4 and 5), indicate different stages of metamorphic (re)equilibration during the D₁/M₁ tectono-metamorphic evolution of the MRC, irrespective of the protolith composition.

Although the possibility that the bulk composition of the chloritoid schists was originally different from that of the graphitic schists cannot be excluded, in the following we propose and discuss two possible mechanisms that could alternatively explain the observed chloritoid zoning: (1) growth-controlled fractionation of chloritoid from a HP/LT (Fe, Mg)-carpholite-bearing assemblage; and (2) fluid ingress driving a change in bulk composition.

(1) Pourteau et al. (2014) showed that extensive, continuous and discontinuous zoning patterns can develop in (Fe, Mg)-chloritoid – carpholite parageneses due to fractionation of elements in the chloritoid cores from the bulk during the metamorphic evolution. Indeed, (Fe, Mg)-carpholite commonly occurs in syn-metamorphic quartz veins in the Verrucano Group metasediments of the TMC (e.g., Theye et al., 1997; Giorgetti et al., 1998; Rossetti et al., 1999; Brogi & Giorgetti, 2012; Giuntoli & Viola, 2021). We could, in principle, infer its former presence also in the MRC. With this assumption, we tested the change in composition of chloritoid with decreasing pressure along an isothermal path as imposed by temperature range estimated via RSCM thermometry (Figure S24). We verified that the continuous fractionation of Fe-rich chloritoid cores in the presence of carpholite produces chloritoid compositions that become progressively richer in Mg with decreasing pressure (compatible with the measured compositions), while carpholite is entirely consumed in the process. At given P and T, the maximum attainable Mg content in chloritoid appears in parageneses with either carpholite or chlorite + pyrophyllite (Figure S24).

(2) There is a striking difference between the investigated chlorite-/chloritoid-schists, containing modal hematite, and graphite schists, which constantly lack ferromagnesian phases (except phengitic muscovite). For example, sample R17 has a bulk composition very similar to that of sample R2 (Table 3), but the former contains chloritoid + hematite, whereas the latter lacks ferromagnesian minerals. This discrepancy cannot be explained simply by differences in composition except differences in $\text{Fe}^{3+}/\text{Fe}^{\text{total}}$. Moreover, according to the thermodynamic modelling, chloritoid and chlorite should have been present at the metamorphic peak also in the graphite-bearing samples (Figure S20).

Notably, the presence of graphite indicates that metamorphism occurred under markedly reducing condition (e.g., French, 1966; Holloway, 1984; Connolly & Cesare, 1993), whereas the presence of metamorphic hematite indicates more oxidizing conditions.

Phase equilibria modelling suggests that the growth of chloritoid- and chlorite-bearing parageneses with the observed composition requires oxidizing conditions with $X_{\text{Fe}_2\text{O}_3}$ values around 0.6 in the chlorite schist (Figure 10b), and 0.1 to 0.35 in the chloritoid schists, respectively (Figure 12b, 15b). Within the temperature range constrained by RSCM thermometry, chloritoid core and rim compositions of sample R6 are both stable in the chloritoid + muscovite + quartz + rutile stability field. However, core compositions require $X_{\text{Fe}_2\text{O}_3}$ close to 0.0 and higher pressures ($P \sim 0.9\text{--}1.3$ GPa), whereas rim compositions are in equilibrium with hematite at $X_{\text{Fe}_2\text{O}_3} \sim 0.1$ for $P \sim 0.6\text{--}1.1$ GPa. The same trend is observed in sample R17, where, for $T = 420$ °C, chloritoid core is stable at $0.6\text{--}1.3$ GPa at $X_{\text{Fe}_2\text{O}_3} = 0.3$, whereas rim compositions require $X_{\text{Fe}_2\text{O}_3}$ values up to 0.7 at $P \sim 0.5\text{--}0.7$ GPa. Another observation that supports this scenario is the observed composition of muscovite. Indeed, the muscovite Si isopleths generally overlap with the X_{Mg} isopleths for chloritoid, whereas the X_{Fe} isopleths of muscovite do not. In all cases, we were never able to reproduce the observed X_{Fe} composition of muscovite ($X_{\text{Fe}} \sim 0.6\text{--}0.7$), neither for reducing nor for oxidizing conditions. This could be in part related to the solution models of white mica (Forshaw & Pattison, 2021). However, it is also possible that muscovite formed earlier and at different conditions than chloritoid, as supported by microstructures indicating syn- to post-kinematic growth of chloritoid on the muscovite-defined foliation (e.g., Figure 5b, c). In this regard, the thermodynamic modelling of chloritoid-bearing samples constrains stability of ferriferous muscovite compositions ($X_{\text{Fe}} > 0.5\text{--}0.6$) to $T < \sim 360\text{--}380$ °C, indicating that muscovite likely grew during the prograde path at reducing conditions (as in the graphite-bearing schists), before the thermal peak was attained in the MRC. This hypothesis is also supported by the negligible differences in syn-metamorphic white mica chemistry that we observe in graphite- and chlorite/chloritoid-bearing schists (Figure 6a-f). Metamorphism under increasingly oxidizing conditions may thus potentially explain the syn- to post-kinematic

chloritoid growth, the observed chloritoid zoning, and the discrepancy between muscovite and chloritoid composition. Beach & Fyfe (1972), Fyfe & Kerrich (1985) reported examples of fluid-mediated changes in the redox conditions during regional metamorphism and thrusting in the ductile crust. Remarkably, we noted that the investigated chloritoid schists are from outcrops preserving pervasive veining and D₁ top-to-the-E shear zones, which might have acted as fluid infiltration pathways within the MRC (e.g., Figure 3c, e). In this scenario, the lack of chloritoid in graphite-bearing samples might be related to the lack of or limited interaction with external fluids (low water/rock ratio) during progress of the Alpine D₁/M₁ tectono-metamorphic evolution. Likewise, the variable celadonite contents in micas of the graphite schists (Fig. 6a-c) indicate that chemical equilibrium is not established on a thin section scale within the MRC during the D₁/M₁ event. This reconstruction is compatible with that depicted by Vidal et al. (2006) for the Sambagawa metamorphic belt (Japan), who noted that at low-grade metamorphic conditions the white mica compositions did not re-equilibrate significantly to changes in the P-T-redox conditions unless their growth was syn-tectonic relative to shear deformation.

We acknowledge that the currently available data cannot firmly constrain any of these models, whose validation is also hampered by the limitation of thermodynamic modelling to precisely reproduce phase equilibria in low-T environments. However, since we found no evidence of (Fe, Mg)-carpholite relics preserved in the metasediments of the MRC, we believe that a fluid-mediated change in the reactive bulk rock composition during progress of the regional low-grade metamorphism explains feasibly the observed zoning patterns of chloritoid as well as the chloritoid blastesis in the MRC.

9.4 Implications at regional scale

Our study shows that the MRC, the southernmost outcrop of the TMC of the Northern Apennines, was involved in the Alpine HP-LT tectono-metamorphic evolution that accompanied the Cenozoic orogenic construction of the Apennine chain. In particular, the P-T deformation history as reconstructed from the MRC may contribute to elucidate the nature of the Paleozoic basement of the Adria continental plate, the P-T regimes and the deep structures responsible for crustal shortening in the hinterland of the northern Apennine chain.

The tectono-metamorphic evolution reconstructed from the exhumed Paleozoic basement section of the TMC exposed in the MRC, where we report a unique Alpine tectono-metamorphic fabric (S1-L1 tectonites; D₁/M₁ event), excludes the presence of a Variscan inheritance in the area. The modelled chloritoid- and chlorite-bearing parageneses and RSCM thermometry allowed to constrain the P-T conditions during the Alpine D₁/M₁ event in the MRC to 0.6 – 1.2 GPa and 375 – 420 °C. The RSCM thermometry (Figure 2, 8; Table 4) shows that the MRC attained a uniform thermal structure, with no evidence of a thermal release during the exhumation path.

If we assume a mean rock density of 2600 kg/m³, the estimated peak pressures indicate maximum depths of ~ 40 km, corresponding to paleo-geothermal gradients of ~ 10 °C/km, compatible with the thermal environments of subduction, as derived from the global record of the Phanerozoic fossil subduction zones (Agard et al., 2018; Penniston-Dorland et al., 2015). The metamorphic estimates derived from the MRC are thus consistent with studies that have documented similar Alpine, HP-LT subduction zone metamorphism in TMC units of the Northern Apennines (Theye et al., 1997; Giorgetti et al., 1998; Jolivet et al., 1998b; Rossetti et al., 1999; Molli et al., 2000; Lo Pò & Braga, 2014; Papeschi et al., 2020; Ryan et al., 2021).

The preservation of a NE-verging, D₁/M₁ thrusting event in the MRC supports the scenario of HP, basement involved, thrusting and nappe stacking during the early stages of the continental collision as documented in the TMC of the Alpi Apuane (Carmignani & Kligfield, 1990; Molli et al. 2000) (Figure 1a). Consequently, the HP-LT D₁/M₁ tectono-metamorphic evolution documented in this study can be linked to the underplating of the Adria plate following the Eocene consumption of the Liguro-Piemontese branch of the Tethyan ocean below the European margin (Vitale Brovarone & Herwartz, 2013) along the west-dipping Apennine-Maghrebian subduction zone (e.g., Jolivet et al., 2003; Faccenna et al., 2004; Malusà et al., 2015).

Significantly, we found no evidence of a post-burial HT metamorphic overprint that would indicate a later thermal overprint in the exhumed MRC and that would support post-orogenic exhumation (e.g., Platt, 1993; Rossetti et al., 1999; Jolivet & Patriat, 1999) as proposed in other areas of the northern Apennines (e.g., Carmignani & Kligfield, 1990; Carmignani et al., 1994; Smith et al., 2011). Consequently, we conclude that exhumation was largely completed before the onset of HT metamorphism in the inner Northern Apennines, consistently with previous evidence (Storti et al., 1995; Jolivet et al., 1998b; Rossetti et al., 1999; Molli et al., 2000; Carosi et al., 2004) and recent studies (Papeschi et al., 2020; Ryan et al., 2021). The cold thermal gradients of the Alpine metamorphism during continuous convergence allowed preservation of the HP parageneses at regional scale. A syn-orogenic exhumation scenario (e.g., Platt, 1986; Jolivet et al., 2003; Warren, 2012) during the construction of the Apennine orogenic wedge is therefore the most appropriate setting to frame the exhumation of the MRC and the other Alpine HP units of the TMC.

10. Conclusions

The following main conclusions arise from the present study:

1. The MRC preserves an Alpine HP/LT D₁/M₁ tectono-metamorphic evolution with cold geothermal conditions (~ 10 °C/km), typical of subduction zone metamorphism (380 – 420 °C and 0.7 – 1.1 GPa), associated to the Apennine orogenic construction;
2. The Alpine D₁/M₁ event is recorded by the blastesis of chloritoid with pronounced core-to-rim X_{Mg} zoning (0.13 to 0.27). Since no evidence of carpholite relics has been documented in the metasediments of the MRC, compositional zoning in chloritoid was likely regulated by a fluid-mediated variation of the reactive bulk rock composition during progress of deformation and metamorphism;
3. Top-to-the-NE ductile shearing accommodated orogenic shortening in the Adria continental crust during construction of the Apennine belt;
4. The tectono-metamorphic evolution of the MRC further confirms that exhumation of the orogenic roots of the Apennine orogen dominantly occurred during active convergence (syn-orogenic exhumation).

Acknowledgements

We thank Moritz Schmelz for help in thin section preparation. We also thank Alessandro Vona for assistance with Raman spectroscopy, and Piergiorgio Scarlato and Manuela Nazzari for assistance and support with electron microprobe analyses at INGV. The manuscript benefited from the constructive reviews of Alicia Lopez-Carmona and an anonymous reviewer that greatly contributed to improve the manuscript. We are grateful to the journal editor Bernardo Cesare for his accurate and constructive comments on the revised version.

Repository

The dataset associated with the present article can be downloaded at
<http://dx.doi.org/10.17632/knrkh9cncr4.3>

Appendix A. Methods and Analytical Techniques

Structural analysis

We analyzed and plotted the collected structural using the software DAISY (<http://host.uniroma3.it/progetti/fralab/Downloads/Programs/>), stereonet 11 (<https://www.rickallmendinger.net/stereonet>), and OpenStereo (<http://igc.usp.br/openstereo/download/>).

Petrography, mineral and whole-rock chemistry

We collected about 50 samples, representative of the observed lithologies and structures (location shown in Figure 2). Oriented thin sections were realized by cutting samples perpendicularly to the foliation and parallel to the stretching lineation (i.e. XZ plane of the finite-strain ellipsoid; Ramsay & Huber, 1987; Passchier & Trouw, 2006) or perpendicularly to the intersection lineation where crenulations were visible.

We carried out preliminary petrographic observations and phase identification using transmitted-light microscopy at the Department of Earth Sciences (University Roma Tre) and X-ray diffraction (XRD) using a Bruker D8 Advance diffractometer at the Institute für Mineralogie und Kristallchemie (University of Stuttgart), operating in θ - 2θ mode.

The chemical composition of minerals in the selected samples, representative of the observed metamorphic parageneses was determined using a CAMECA SX100 and a JEOL JXA 8200 electron microprobe (EMP) analyzers, both equipped with five WDS spectrometers and EDS systems, respectively installed at the Institut für Mineralogie und

Kristallchemie (University of Stuttgart) and at the HP-HT Laboratory of Experimental Volcanology and Geophysics of the Istituto Nazionale di Geofisica e Vulcanologia (INGV, Rome). Analytical conditions for spot analyses were 15 kV accelerating voltage, 10 – 20 nA beam current, 20 s counting time on peak and 10–20 s on background, and 1–5 μm spot size (average: 2 μm); defocused beam sizes were used to avoid alkali-loss in micas. The standards used were wollastonite and jadeite (Si), wollastonite and augite (Ca), corundum (Al), iron(III) oxide and andradite (Fe), rhodonite (Mn), manganese(II) titanate and rutile (Ti), albite (Na), orthoclase (K), forsterite (Mg) and barite (Ba). White mica (muscovite and paragonite) and chlorite analyses were recalculated on 11 and 14 O basis, respectively, assuming all iron to be divalent. Chloritoid was recalculated on a 12 O basis and its Fe^{3+} was recalculated based on a cation sum of 8. We used Calcmn v. 3.2 (Brandelik, 2009) to process microprobe data (.cor files). We recalculated phyllosilicate endmembers using the chlorite model by Vidal & Parra (2000) and the white mica model by Massonne (1992). Concentration maps for major elements (Ca, Fe, Mn, Mg, Al, Na) were acquired by stepwise movements of the thin section under the electron beam with 100 ms counting times per step. Analyses collected at INGV are indicated by a prefix “a-” in the Supplementary Figures S3-S15 as well as in the repository associated with the present article (<http://dx.doi.org/10.17632/knrkh9cncr4.2>).

Major elemental composition (Si, Al, Fe, Mg, Mn, Ca, Na, K, Ti) of six selected samples was determined by X-ray fluorescence spectroscopy (XRF) using a Panalytical PW2400 spectrometer at the Institut für Mineralogie und Kristallchemie at Universität Stuttgart. Loss on ignition (LOI) was determined by heating to 850°C. For the measured elements the precision is estimated better than 2% for values higher than 5 wt% and better than 5% in the range 0.1–5 wt%.

Selected samples of graphite schists, distributed over the MRC, were used to estimate peak metamorphic temperatures through RSCM thermometry. We obtained Raman spectra using a Horiba Jobin Yvon LABRAM HR800 (*Università di Roma Tre*), equipped with a CCD detector operating at -70 °C and an Olympus reflected light microscope. We used a 514 nm (green) laser focused on the sample with a 100x objective. The laser power on the sample surface was set at 1 mW. The Rayleigh diffusion was eliminated by edge filters, and to achieve nearly confocal configuration the entrance slit was closed down to 15 µm. The signal was finally dispersed using a 1800 gr/mm grating and analyzed by a Peltier cooled CCD detector. Before each session, we calibrated the spectrometer – operated through the Labspec 5 software – with a silicon standard. In order to avoid analytical mismatch, we followed the analytical and fitting procedures of Beyssac, Goffé, Chopin, & Rouzaud (2002) and Beyssac et al. (2003). We recorded between 9 and 20 spectra (average: 14) for each sample, based on the available amount of carbonaceous material (CM), with average acquisition times of 120 s. The sample was measured over a spectral window of 1000 to 2000 cm^{-1} ; replicate analyses over a larger spectral window (700 to 2300 cm^{-1}) indicate that the smaller window was of sufficient size to estimate the baseline for the spectra. These spectra were acquired over areally distributed points, in order to eliminate the effect of eventual micro-heterogeneities. Spectra were then processed using the software Peakfit 4.12, using the Voigt elaboration function and subtracting a quadratic baseline from each spectrum. In order to estimate peak metamorphic temperature in samples of graphite schists, the calibration of Beyssac et al. (2002) was adopted, as Raman spectra lack an appreciable D4 band, characteristic of CM in very low-grade metamorphic rocks, at temperatures typically below 330 °C (Lahfid et al., 2010). The RSCM geothermometer has an absolute precision of ± 50 °C due to uncertainties

on petrological data used for the calibration. Relative uncertainties on each measured temperature are smaller, in the range of 10–15 °C (Beyssac et al., 2004).

References

Agard, P., Vidal, O., & Goffé, B. (2001). Interlayer and Si content of phengite in HP–LT carpholite-bearing metapelites. *Journal of Metamorphic Geology*, 19(5), 479-495.

Agard, P., Labrousse, L., Elvevold, S., & Lepvrier, C. (2005). Discovery of Paleozoic Fe-Mg carpholite in Motalafjella, Svalbard Caledonides: A milestone for subduction-zone gradients. *Geology*, 33(10), 761-764.

Agard, P., Monié, P., Gerber, W., Omrani, J., Molinaro, M., Meyer, B., Labrousse, L., Vrielynck, B., Jolivet, L. & Yamato, P. (2006). Transient, synobduction exhumation of Zagros blueschists inferred from P–T, deformation, time and kinematic constraints: Implications for Neotethyan wedge dynamics. *Journal of Geophysical Research* 111, B11401, doi:10.1029/2005JB004103.

Agard, P., Yamato, P., Jolivet, L., & Burov, E. (2009). Exhumation of oceanic blueschists and eclogites in subduction zones: timing and mechanisms. *Earth-Science Reviews*, 92(1-2), 53-79.

Agard, P., Plunder, A., Angiboust, S., Bonnet, G., & Ruh, J. (2018). The subduction plate interface: rock record and mechanical coupling (from long to short timescales). *Lithos*, 320, 537-566.

Alberti, A., Bertini, M., Del Bono, G. L., & Salvati, L. (1970). Note illustrative della Carta Geologica d'Italia alla scala 1: 100.000–Foglio 136 Tuscania–Foglio 142

Civitavecchia. *Poligrafica & Cartevalori, Ercolano (NA)*.

Aldinucci, M., Gandin, A., & Sandrelli, F. (2008). The Mesozoic continental rifting in the Mediterranean area: insights from the Verrucano tectofacies of southern Tuscany (Northern Apennines, Italy). *International Journal of Earth Sciences*, 97(6), 1247-1269.

Alvarez, W., Coccozza, T., & Wezel, F. C. (1974). Fragmentation of the Alpine orogenic belt by microplate dispersal. *Nature*, 248(5446), 309-314.

Andersen, D. J., & Lindsley, D. H. (1988). Internally consistent solution models for Fe-Mg-Mn-Ti oxides; Fe-Ti oxides. *American Mineralogist*, 73(7-8), 714-726.

Angiboust, S., Agard, P., Raimbourg, H., Yamato, P., & Huet, B. (2011). Subduction interface processes recorded by eclogite-facies shear zones (Monviso, W. Alps). *Lithos*, 127(1-2), 222-238.

Angiboust, S., Kirsch, J., Oncken, O., Glodny, J., Monié, P., & Rybacki, E. (2015). Probing the transition between seismically coupled and decoupled segments along an ancient subduction interface. *Geochemistry, Geophysics, Geosystems*, 16(6), 1905-1922.

Azañón, J. M., García-Dueñas, V., & Goffé, B. (1998). Exhumation of high-pressure metapelites and coeval crustal extension in the Alpujarride complex (Betic Cordillera). *Tectonophysics*, 285(3-4), 231-252.

Azzaro, E., & Di Sabatino, B. (1974). Prime indagini su alcuni affioramenti di serie metamorfiche dei Monti Romani (Lazio settentrionale). *Periodico di Mineralogia*, 43(1), 161-173.

Azzaro, E., Di Sabatino, B., & Negretti, G. (1975). Considerazioni petrologiche sugli «scisti violetti» del settore Argentario-Monti Romani (Toscana Meridionale-Lazio Settentrionale). *Period. Mineral*, 44, 305-317.

Beach, A., & Fyfe, W. S. (1972). Fluid transport and shear zones at Scourie, Sutherland: evidence of overthrusting?. *Contributions to Mineralogy and Petrology*, 36(3), 175-180.

Bebout, G.E., Penniston-Dorland, S.C. (2016). Fluid and mass transfer at subduction interfaces—the field metamorphic record. *Lithos*, 240-243, 228-258, 10.1016/j.lithos.2015.10.007.

Berthé, D., Choukroune, P., & Jégouzo, P. (1979). Orthogneiss, mylonite and non coaxial deformation of granites: the example of the South Armorican Shear Zone. *Journal of Structural Geology*, 1(1), 31-42.

Bertini, G., Casini, M., Gianelli, G., & Pandeli, E. (2006). Geological structure of a long-living geothermal system, Larderello, Italy. *Terra Nova*, 18(3), 163-169.

Beyssac, O., Goffé, B., Chopin, C., & Rouzaud, J. N. (2002). Raman spectra of carbonaceous material in metasediments: a new geothermometer. *Journal of metamorphic Geology*, 20(9), 859-871.

Beyssac, O., Goffé, B., Petitet, J. P., Froigneux, E., Moreau, M., & Rouzaud, J. N. (2003). On the characterization of disordered and heterogeneous carbonaceous materials by Raman spectroscopy. *Spectrochimica Acta Part A: Molecular and Biomolecular Spectroscopy*, 59(10), 2267-2276.

Beyssac, O., Bollinger, L., Avouac, J. P., & Goffé, B. (2004). Thermal metamorphism in the lesser Himalaya of Nepal determined from Raman spectroscopy of carbonaceous material. *Earth and Planetary Science Letters*, 225(1-2), 233-241.

Bianco, C., Brogi, A., Caggianelli, A., Giorgetti, G., Liotta, D., & Meccheri, M. (2015). HP-LT metamorphism in Elba Island: implications for the geodynamic evolution of the inner Northern Apennines (Italy). *Journal of Geodynamics*, 91, 13-25.

Bianco, C., Godard, G., Halton, A., Brogi, A., Liotta, D., & Caggianelli, A. (2019). The lawsonite-glaucophane blueschists of Elba Island (Italy). *Lithos*, 348-349, 105198.

Black, P.M., Maurizot, P., Ghent, E.D., Stout, M.Z. (1993). Mg-Fe carpholite from aluminous schists in the Diahot region and implications for preservation of high-

pressure/low-temperature schists, northern New Caledonia. *Journal of Metamorphic Geology*, 11, 455-460.

Boccaletti, M., Elter, P., & Guazzone, G. (1971). Plate tectonic models for the development of the Western Alps and Northern Apennines. *Nature Physical Science*, 234(49), 108-111.

Bonini, M., Sani, F., Stucchi, E. M., Moratti, G., Benvenuti, M., Menanno, G., & Tanini, C. (2014). Late Miocene shortening of the Northern Apennines back-arc. *Journal of Geodynamics*, 74, 1-31.

Bossio, A., Costantini, A., Foresi, L. M., Lazzarotto, A., Mazzanti, R., Mazzei, R., ... Terzuoli, A. (1998). Neogene-Quaternary sedimentary evolution in the Western side of the Northern Apennines (Italy). *Mem. Soc. Geol. It.*, 52, 513-525.

Bousquet, R., Goffé, B., Vidal, O., Oberhänsli, R., & Patriat, M. (2002). The tectono-metamorphic history of the Valaisan domain from the Western to the Central Alps: New constraints on the evolution of the Alps. *Geological Society of America Bulletin*, 114(2), 207-225.

Bouybaouene, M. L., Goffé, B., & Michard, A. (1995). High-pressure, low-temperature metamorphism in the Septides nappes, northern Rif, Morocco.

Brandelik, A. (2009). CALCMIN—an EXCEL™ Visual Basic application for calculating mineral structural formulae from electron microprobe analyses. *Computers & Geosciences*, 35(7), 1540-1551.

Brogi, A., & Giorgetti, G. (2012). Tectono-metamorphic evolution of the siliciclastic units in the Middle Tuscan Range (inner Northern Apennines): Mg–carpholite bearing quartz veins related to syn-metamorphic syn-orogenic foliation. *Tectonophysics*, 526, 167-184.

Brunet, C., Monié, P., Jolivet, L., & Cadet, J. P. (2000). Migration of compression and extension in the Tyrrhenian Sea, insights from $^{40}\text{Ar}/^{39}\text{Ar}$ ages on micas along a transect from Corsica to Tuscany. *Tectonophysics*, 321(1), 127-155.

Burckhardt, C. E. (1946), Il sondaggio di Belagajo (Grosseto) ed il suo significato geologico, *Boll. Soc. Geol. Ital.*, LXV, 98 – 107.

Capezzuoli, E., Spina, A., Brogi, A., Liotta, D., Bagnoli, G., Zucchi, M., ... & Regoli, R. (2021). Reconsidering the Variscan basement of southern Tuscany (inner Northern Apennines). *Geosciences*, 11(2), 84.

Cao, S., Neubauer, F., Bernroider, M., & Genser, J. (2018). Eocene high-pressure metamorphism and Oligocene retrogression on Naxos, Cyclades, Greece: Significance for Aegean tectonics and $^{40}\text{Ar}/^{39}\text{Ar}$ dating in polyphase metamorphic rocks. *Tectonophysics*, 745, 66-94.

Carmignani, L., & Kligfield, R. (1990). Crustal extension in the Northern Apennines: the transition from compression to extension in the Alpi Apuane core complex. *Tectonics*, 9(6), 1275-1303.

Carmignani, L., Decandia, F. A., Fantozzi, P. L., Lazzarotto, A., Liotta, D., & Meccheri, M. (1994). Tertiary extensional tectonics in Tuscany (Northern Apennines, Italy). *Tectonophysics*, 238(1-4), 295-315.

Carosi, R., Leoni, L., Montomoli, C., & Sartori, F. (2003). Very low-grade metamorphism in the Tuscan Nappe, Northern Apennines, Italy: relationships between deformation and metamorphic indicators in the La Spezia mega-fold. *Swiss Bulletin of Mineralogy and Petrology*, 83(1), 15-32.

Carosi, R., Montomoli, C., & Pertusati, P. C. (2004). Late tectonic evolution of the Northern Apennines: the role of contractional tectonics in the exhumation of the Tuscan units. *Geodinamica Acta*, 17(4), 253-273.

Carreras, J., & Druguet, E. (1994). Structural zonation as a result of inhomogeneous non-coaxial deformation and its control on syntectonic intrusions: an example from the Cap de Creus area, eastern-Pyrenees. *Journal of Structural Geology*, 16(11), 1525-1534.

Cassinis, G., Perotti, C., & Santi, G. (2018). Post-Variscan Verrucano-like deposits in Italy, and the onset of the alpine tectono-sedimentary cycle. *Earth-Science Reviews*, 185, 476-497.

Cathelineau, M. (1988). Cation site occupancy in chlorites and illites as a function of temperature. *Clay minerals*, 23(4), 471-485.

Cerrina Feroni, A., Ottria, G., Martinelli, P., & Martelli, L., (2002). Carta Geologico-Strutturale dell'Appennino Emiliano-Romagnolo. Scala 1:250.000, Regione Emilia-Romagna, C.N.R., Bologna.

Chopin, C. (1984). Coesite and pure pyrope in high-grade blueschists of the western Alps: a first record and some consequences. *Contributions to Mineralogy and Petrology*, 86, 107-118.

Cirilli, S., Decandia, F. A., Lazzarotto, A., Pandeli, E., Rettori, R., Sandrelli, F., & Spina, A. (2002). Stratigraphy and depositional environment of the Mt. Argentario sandstones (southern Tuscany, Italy). *Bollettino della Società Geologica Italiana, Special Volumes, 1*, 489-498.

Clemenzi, L., Molli, G., Storti, F., Muchez, P., Swennen, R., & Torelli, L. (2014). Extensional deformation structures within a convergent orogen: the Val di Lima low-angle normal fault system (Northern Apennines, Italy). *Journal of Structural Geology*, 66, 205-222.

Cocozza, T., Gasperi, G., Gelmini, R., & Lazzarotto, A. (1974). Segnalazione di nuovi affioramenti paleozoici (Permo-Carbonifero?) a Boccheggiano e tra Capalbino e i Monti Romani (Toscana meridionale-Lazio settentrionale). *Boll.Soc.Geol.It.*, 93, 47-60

Connolly, J. A. (2005). Computation of phase equilibria by linear programming: a tool for geodynamic modeling and its application to subduction zone decarbonation. *Earth and Planetary Science Letters*, 236(1-2), 524-541.

Connolly, J. A. D. (2009). The geodynamic equation of state: what and how. *Geochemistry, Geophysics, Geosystems*, 10(10).

Connolly, J. A. D., & Cesare, B. (1993). C-O-H-S fluid composition and oxygen fugacity in graphitic metapelites. *Journal of metamorphic geology*, 11(3), 379-388.

Connolly, J. A. D., & Kerrick, D. M. (2002). Metamorphic controls on seismic velocity of subducted oceanic crust at 100–250 km depth. *Earth and Planetary Science Letters*, 204(1-2), 61-74.

Conti, P., Costantini, A., Decandia, F. A., Elter, F. M., Gattiglio, M., Lazzarotto, A., ... & Di Pisa, A. (1991). Structural frame of the Tuscan Paleozoic: a review. *Bollettino della Società Geologica Italiana*, 110(3-4), 523-541.

Conti, P., Di Pisa, A., Gattiglio, M., & Meccheri, M. (1993). The pre-alpine basement in the Alpi Apuane (Northern Apennines, Italy). In *Pre-Mesozoic geology in the Alps* (pp. 609-621). Springer, Berlin, Heidelberg.

Conti, P., Cornamusini, G., & Carmignani, L. (2020). An outline of the geology of the Northern Apennines (Italy), with geological map at 1: 250,000 scale. *Italian Journal of Geosciences*, 139(2), 149-194.

Cook-Kollars, J., Bebout, G. E., Collins, N. C., Angiboust, S., & Agard, P. (2014).

Subduction zone metamorphic pathway for deep carbon cycling: I. Evidence from HP/UHP metasedimentary rocks, Italian Alps. *Chemical Geology*, 386, 31-48.

Cosentino, D., Cipollari, P., Marsili, P., & Scrocca, D. (2010). Geology of the central Apennines: a regional review. *Journal of the Virtual Explorer*, 36(11), 1-37.

Curzi, M., Billi, A., Carminati, E., Rossetti, F., Albert, R., Aldega, L., Cardello, L.G., Conti, A. Gerdes, A., Smeraglia, L., Van der Lelij, L., Vignaroli, G., & Viola, G. (2020). Disproving the presence of Paleozoic-Triassic metamorphic rocks on the Island of Zannone (central Italy): Implications for the early stages of the Tyrrhenian-Apennines tectonic evolution. *Tectonics*, e2020TC006296.

Dallan Nardi, L., & Nardi, R., (1972) - Schema stratigrafico e strutturale dell'Appennino settentrionale. *Memorie dell'Accademia Lunigianese di Scienze*, 42, 212 pp.

Decandia, F.A., & Lazzarotto, A. (1980) - Le unità tettoniche del Monte Argentario (Toscana Meridionale). *Memorie della Società Geologica Italiana*, 21, 385-393.

Deino, A., Keller, J.V.A., Minelli, G., & Piali, G. (1992). Datazioni $^{40}\text{Ar}/^{39}\text{Ar}$ del metamorfismo dell'Unità di Ortano-Rio Marina (Isola d'Elba): risultati preliminari. *Studi Geologici Camerti* 2, 187–192.

Dessau, G. (1951). Geologia e depositi di Antimonio e d'altri minerali del Gruppo dei Monti Romani (Comune di Manciano, Maremma Toscana). *Boll.Soc.Geol.It.*, 70, 1-64.

Dessau, G. (1952). Antimony deposits of Tuscany. *Economic Geology*, 47(4), 397-413.

Dessau, G., Duchi, G., & Stea, B. (1972). Geologia e depositi minerari della zona dei Monti Romani – Monteti (Comune di Manciano) e Capalbio (Grosseto) e Ischia di Castro (Viterbo). *Memorie della Società Geologica Italiana*, 11, 217-260

Dewey, J. F. (1988). Extensional collapse of orogens. *Tectonics*, 7(6), 1123-1139.

Di Rosa, M., De Giorgi, A., Marroni, M., & Vidal, O. (2017). Syn-convergence exhumation of continental crust: evidence from structural and metamorphic analysis of the Monte Cecu area, Alpine Corsica (Northern Corsica, France). *Geological Journal*, 52(6), 919-937.

Diener, J. F. A., & R. Powell (2012). Revised activity–composition models for clinopyroxene and amphibole. *Journal of Metamorphic Geology*, 30(2), 131-142.

Doglioni, C., Gueguen, E., Sàbat, F., & Fernandez, M. (1997). The western Mediterranean extensional basins and the Alpine orogen. *Terra Nova*, 9(3), 109-112.

Elter, P., 1975. Introduction a` la géologie de l'Apennin septentrional. *Bull. Soc. Geol. Fr.* 7, 956–962.

Elter, P., & Marroni, M., (1991). Le Unità Liguri dell'Appennino settentrionale: sintesi dei dati e nuove interpretazioni. *Memorie Descrittive della Carta Geologica d'Italia*, 46, 121–138.

Elter, G., Elter, P., Sturani, C., & Weidmann, M., 1966. Sur la prolongation du domaine ligure de l'Apennin dans le Monferrat et les Alpes et sur l'origine de la Nappe de la Simme s.l. et des Préalps romande et chablasiennes. *Archives Science Geneve*, 19, 279–377.

Epstein, G. S., Bebout, G. E., Angiboust, S., & Agard, P. (2020). Scales of fluid-rock interaction and carbon mobility in the deeply underplated and HP-Metamorphosed Schistes Lustrés, Western Alps. *Lithos*, 354, 105229.

Ernst, W.G. (1971). Metamorphic zonations on presumably subducted lithospheric plates from Japan, California, and the Alps. *Contributions to Mineralogy and Petrology*, 34, 43-59

Ernst, W. G., & Dal Piaz, G. V. (1978). Mineral parageneses of eclogitic rocks and related mafic schists of the Piemonte ophiolite nappe, Breuil-St. Jacques area, Italian Western Alps. *American Mineralogist*, 63(7-8), 621-640.

Escher, A., & Beaumont, C. (1997). Formation, burial and exhumation of basement nappes at crustal scale: a geometric model based on the Western Swiss-Italian Alps. *Journal of Structural Geology*, 19(7), 955-974.

Faccenna, C., Funicello, F., Giardini, D., & Lucente, P. (2001). Episodic back-arc extension during restricted mantle convection in the Central Mediterranean. *Earth and Planetary Science Letters*, 187(1-2), 105-116.

Faccenna, C., Piromallo, C., Crespo-Blanc, A., Jolivet, L., & Rossetti, F. (2004). Lateral slab deformation and the origin of the western Mediterranean arcs. *Tectonics*, 23(1).

Forshaw, J. B., & Pattison, D. R. (2021). Ferrous/ferric ($\text{Fe}^{2+}/\text{Fe}^{3+}$) partitioning among silicates in metapelites. *Contributions to Mineralogy and Petrology*, 176(9), 1-26.

Franceschelli, M., & Memmi, I. (1999). Zoning of chloritoid from kyanite-facies metapsammities, Alpi Apuane, Italy. *Mineralogical Magazine*, 63(1), 105-110.

Franceschelli, M., Leoni, L., Memmi, I., & Puxeddu, M. (1986). Regional distribution of Al-silicates and metamorphic zonation in the low-grade Verrucano metasediments from the Northern Apennines, Italy. *Journal of Metamorphic Geology*, 4(3), 309-321.

Franceschelli, M., Memmi, I., Carcangiu, G., & Gianelli, G. (1997). Prograde and retrograde chloritoid zoning in low temperature metamorphism, Alpi Apuane, Italy.

Franceschelli, M., Gianelli, G., Pandeli, E., & Puxeddu, M. (2004). Variscan and Alpine metamorphic events in the Northern Apennines (Italy): a review. *Periodico di Mineralogia*, 73(2), 43-56.

French, B. M. (1966). Some geological implications of equilibrium between graphite and a C-H-O gas phase at high temperatures and pressures. *Reviews of Geophysics*, 4(2), 223-253.

Frezzotti, M. L., Selverstone, J., Sharp, Z. D., & Compagnoni, R. (2011). Carbonate dissolution during subduction revealed by diamond-bearing rocks from the Alps. *Nature Geoscience*, 4(10), 703-706.

Fuhrman, M. L., & Lindsley, D. H. (1988). Ternary-feldspar modeling and thermometry. *American mineralogist*, 73(3-4), 201-215.

Funiciello, R., Salvini, F., & Wise, D. U. (1984). Deformational history of basement exposures along the Fiora river, central Italy. *Bollettino della Società geologica italiana*, 103(3), 491-501.

Fyfe, W. S., & Kerrich, R. (1985). Fluids and thrusting. *Chemical Geology*, 49(1-3), 353-362.

Giorgetti, G., Goffe, B., Memmi, I., & Nieto, F. (1998). Metamorphic evolution of Verrucano metasediments in Northern Apennines; new petrological constraints. *European Journal of Mineralogy*, 10(6), 1295-1308.

Giuntoli, F., & Viola, G. (2021). Cyclic brittle-ductile oscillations recorded in exhumed high-pressure continental units: A record of deep episodic tremor and slow slip events in the Northern Apennines. *Geochemistry, Geophysics, Geosystems*, e2021GC009805.

Goffé, B., Michard, A., Kienast, J. R., & Le Mer, O. (1988). A case of obduction-related high-pressure, low-temperature metamorphism in upper crustal nappes, Arabian continental margin, Oman: PT paths and kinematic interpretation. *Tectonophysics*, 151(1-4), 363-386.

Goffé, B., & Chopin, C. (1986). High-pressure metamorphism in the Western Alps: zoneography of metapelites, chronology and consequences. *Schweizerische Mineralogische und Petrographische Mitteilungen*, 66, 41-52.

Green, E., Holland, T., & Powell, R. (2007). An order-disorder model for omphacitic pyroxenes in the system jadeite-diopside-hedenbergite-acmite, with applications to eclogitic rocks. *American Mineralogist*, 92(7), 1181-1189.

- Holland, T. J. B., & Powell, R. (1998). An internally consistent thermodynamic data set for phases of petrological interest. *Journal of metamorphic Geology*, 16(3), 309-343.
- Holland, T. J. B., & Powell, R. (2001). Calculation of phase relations involving haplogranitic melts using an internally consistent thermodynamic dataset. *Journal of Petrology*, 42(4), 673-683.
- Holloway, J. R. (1984). Graphite-CH₄-H₂O-CO₂ equilibria at low-grade metamorphic conditions. *Geology*, 12(8), 455-458.
- Jolivet, L., & Patriat, M. (1999). Ductile extension and the formation of the Aegean Sea. *Geological Society, London, Special Publications*, 156(1), 427-456.
- Iannace, A., Vitale, S., D'Errico, M., Mazzoli, S., Di Staso, A., Macaione, E., Messina, A., Reddy, S. M., Somma, R., Zamparelli, V., Zattin, M., Bonardi, G. (2007). The carbonate tectonic units of northern Calabria (Italy): a record of Apulian palaeomargin evolution and Miocene convergence, continental crust subduction, and exhumation of HP-LT rocks. *Journal of the Geological Society*, 164 (6), 1165-1186.
- Jolivet, L., & Faccenna, C. (2000). Mediterranean extension and the Africa-Eurasia collision. *Tectonics*, 19(6), 1095-1106.
- Jolivet, L., Goffé, B., Bousquet, R., Oberhänsli, R., & Michard, A. (1998a). Detachments in high-pressure mountain belts, Tethyan examples. *Earth and Planetary Science Letters*, 160(1-2), 31-47.

Jolivet, L., Faccenna, C., Goffé, B., Mattei, M., Rossetti, F., Brunet, C., Storti, F., Funiciello, R., Cadet, J.P., D'Agostino N., & Parra, T. (1998b). Midcrustal shear zones in postorogenic extension: example from the northern Tyrrhenian Sea. *Journal of Geophysical Research: Solid Earth*, 103(B6), 12123-12160.

Jolivet, L., Faccenna, C., Goffé, B., Burov, E., & Agard, P. (2003). Subduction tectonics and exhumation of high-pressure metamorphic rocks in the Mediterranean orogens. *American Journal of Science*, 303(5), 353-409.

Jowett, E. C. (1991). Fitting iron and magnesium into the hydrothermal chlorite geothermometer. In *GAC/MAC/SEG Joint Annual Meeting, Toronto, May 27-29, 1991, Program with Abstracts 16*.

Keller, J. V. A., & Coward, M. P. (1996). The structure and evolution of the Northern Tyrrhenian Sea. *Geological Magazine*, 133(1), 1-16.

Kligfield, R., Hunziker, J., Dallmeyer, R. D., & Schamel, S. (1986). Dating of deformation phases using K-Ar and $^{40}\text{Ar}/^{39}\text{Ar}$ techniques: results from the Northern Apennines. *Journal of Structural Geology*, 8(7), 781-798.

Kotowski, A. J., & Behr, W. M. (2019). Length scales and types of heterogeneities along the deep subduction interface: Insights from exhumed rocks on Syros Island, Greece. *Geosphere*, 15(4), 1038-1065.

Kranidiotis, P., & MacLean, W. H. (1987). Systematics of chlorite alteration at the Phelps Dodge massive sulfide deposit, Matagami, Quebec. *Economic Geology*, 82(7), 1898-1911.

Kryza, R., Willner, A. P., Massonne, H. J., Muszyński, A., & Schertl, H. P. (2011). Blueschist-facies metamorphism in the Kaczawa Mountains (Sudetes, SW Poland) of the Central-European Variscides: PT constraints from a jadeite-bearing metatrachyte. *Mineralogical Magazine*, 75(1), 241-263.

Lahfid, A., Beyssac, O., Deville, E., Negro, F., Chopin, C., & Goffé, B. (2010). Evolution of the Raman spectrum of carbonaceous material in low-grade metasediments of the Glarus Alps (Switzerland). *Terra nova*, 22(5), 354-360.

Lavecchia, G., Minelli, G., & Piali, G., (1984). L'Appennino umbro-marchigiano: tettonica distensiva ed ipotesi di sismogenesi. *Bollettino della Societa' Geologica Italiana*, 103, 467-476.

Lazzarotto, A., Aldinucci, M., Cirilli, S., Costantini, A., Decandia, F. A., Pandeli, E., ... & Spina, A. (2003). Stratigraphic correlation of the Upper Palaeozoic-Triassic successions in southern Tuscany, Italy. *Bollettino della Società Geologica Italiana, Special Volumes*, 2, 25-35.

Lefeuvre, B., Agard, P., Verlaquet, A., Dubacq, B., & Plunder, A. (2020). Massive formation of lawsonite in subducted sediments from the Schistes Lustrés (W. Alps): Implications for mass transfer and decarbonation in cold subduction zones. *Lithos*, 370, 105629.

Lo Pò, D., & Braga, R. (2014). Influence of ferric iron on phase equilibria in greenschist facies assemblages: the hematite-rich metasedimentary rocks from the Monti Pisani (Northern Apennines). *Journal of Metamorphic Geology*, 32(4), 371-387.

Lo Pò, D., Braga, R., Massonne, H. J., Molli, G., Montanini, A., & Theye, T. (2016). Fluid-induced breakdown of monazite in medium-grade metasedimentary rocks of the Pontremoli basement (Northern Apennines, Italy). *Journal of Metamorphic Geology*, 34(1), 63-84.

Locatelli, M., Verlaquet, A., Agard, P., Federico, L., & Angiboust, S. (2018). Intermediate-depth brecciation along the subduction plate interface (Monviso eclogite, W. Alps). *Lithos*, 320, 378-402.

López-Carmona, A., Pitra, P., & Abati, J. (2013). Blueschist-facies metapelites from the Malpica–Tui Unit (NW Iberian Massif): phase equilibria modelling and H₂O and Fe₂O₃ influence in high-pressure assemblages. *Journal of Metamorphic Geology*, 31(3), 263-280.

Lopez-Carmona, A., Abati, J., Pitra, P., & Lee, J. K. (2014). Retrogressed lawsonite blueschists from the NW Iberian Massif: P–T–t constraints from thermodynamic modelling and ⁴⁰Ar/³⁹Ar geochronology. *Contributions to Mineralogy and Petrology*, 167(3), 1-20.

Malinverno, A., & Ryan, W. B. (1986). Extension in the Tyrrhenian Sea and shortening in the Apennines as result of arc migration driven by sinking of the lithosphere. *Tectonics*, 5(2), 227-245.

Malusà, M. G., Faccenna, C., Baldwin, S. L., Fitzgerald, P. G., Rossetti, F., Balestrieri, M. L., ... & Piromallo, C. (2015). Contrasting styles of (U) HP rock exhumation along the Cenozoic Adria-Europe plate boundary (Western Alps, Calabria, Corsica). *Geochemistry, Geophysics, Geosystems*, 16(6), 1786-1824.

Martini, I. P., Cascella, A., & Rau, A. (1995). The Manciano Sandstone: a shoreface deposit of Miocene basins of the Northern Apennines, Italy. *Sedimentary Geology*, 99(1), 37-59.

Marrone, S., Monié, P., Rossetti, F., Lucci, F., Theye, T., Bouybaouene, M. L., & Zaghloul, M. N. (2021). The Pressure-Temperature-time-deformation history of the Beni Mzala unit (Upper Sebtides, Rif belt, Morocco): Refining the Alpine tectono-metamorphic evolution of the Alboran Domain of the Western Mediterranean. *Journal of Metamorphic Geology*, 39(5), 591–615.

Marroni, M., Meneghini, F., & Pandolfi, L. (2010). Anatomy of the Ligure-Piemontese subduction system: evidence from Late Cretaceous–middle Eocene convergent margin deposits in the Northern Apennines, Italy. *International Geology Review*, 52(10-12), 1160-1192.

Massa, G., Musumeci, G., Mazzarini, F., & Pieruccioni, D. (2017). Coexistence of contractional and extensional tectonics during the Northern Apennines orogeny: the late Miocene out-of-sequence thrust in the Elba Island nappe stack. *Geological Journal*, 52(3), 353-368.

Massonne, H. J. (1992). Evidence for low-temperature ultrapotassic siliceous fluids in subduction zone environments from experiments in the system K_2O - MgO - Al_2O_3 - SiO_2 - H_2O (KMASH). *Lithos*, 28(3-6), 421-434.

Massonne, H. J. (2010). Phase relations and dehydration behaviour of calcareous sediments at very-low to low grade metamorphic conditions. *Periodico di Mineralogia*, 79(2), 21-43.

Molli, G., Giorgetti, G., & Meccheri, M. (2000). Structural and petrological constraints on the tectono-metamorphic evolution of the Massa Unit (Alpi Apuane, NW Tuscany, Italy). *Geological Journal*, 35(3-4), 251-264.

Molli, G., Montanini, A., & Frank, W. (2002). MORB-derived Variscan amphibolites in the Northern Apennine basement: The Cerreto metamorphic slices (Tuscan-Emilian Apennine, NW Italy). *Ophioliti*, 27(1), 17-30.

Molli G, & Vaselli L (2006) Structures, interference patterns and strain regime during mid-crustal deformation in the Alpi Apuane (Northern Apennines, Italy). In: Mazzoli S, Butler R (eds) Styles of continental contraction. *Geological Society of America, Spec Pap 414*, 79–93.

Molli, G., Brovarone, A. V., Beyssac, O., & Cinquini, I. (2018). RSCM thermometry in the Alpi Apuane (NW Tuscany, Italy): New constraints for the metamorphic and tectonic history of the inner Northern Apennines. *Journal of Structural Geology*, 113, 200-216.

Molli, G., Brogi, A., Caggianelli, A., Capezzuoli, E., Liotta, D., Spina, A. & Zibra, I. (2020).

Late Palaeozoic tectonics in Central Mediterranean: a reappraisal. *Swiss Journal of Geosciences*, 113, 23. <https://doi.org/10.1186/s00015-020-00375-1>

Moretti, A., Meletti, C., & Ottria, G. (1990). Studio stratigrafico e strutturale dei Monti

Romani (GR-VT)-1: Dal Paleozoico all'orogenesi alpida. *Bollettino della Società geologica italiana*, 109(3), 557-581.

Musumeci, G., Bocini, L., & Corsi, R. (2002). Alpine tectonothermal evolution of the Tuscan Metamorphic Complex in the Larderello geothermal field (Northern Apennines, Italy).

Journal of the Geological Society, 159(4), 443-456.

Musumeci, G., Mazzarini, F., Tiepolo, M., & Di Vincenzo, G. (2011). U-Pb and ⁴⁰Ar-³⁹Ar geochronology of Palaeozoic units in the Northern Apennines: determining protolith age and alpine evolution using the Calamita Schist and Ortano Porphyroid. *Geological Journal*, 46(4), 288-310.

Musumeci, G., Mazzarini, F., & Cruden, A. R. (2015). The Zuccale Fault, Elba Island, Italy: a new perspective from fault architecture. *Tectonics*, 34(6), 1195-1218.

Oberhänsli, R., Partzsch, J., Candan, O., & Cetinkaplan, M. (2001). First occurrence of Fe-Mg-carpholite documenting a high-pressure metamorphism in metasediments of the Lycian Nappes, SW Turkey. *International Journal of Earth Sciences*, 89(4), 867-873.

Pandeli, E., Gianelli, G., & Morelli, M. (2005). The crystalline units of the middle–upper crust of the Larderello geothermal region (southern Tuscany, Italy): new data for their classification and tectono-metamorphic evolution. *Bollettino della Società Geologica Italiana, Special Volume, 3*, 136-159.

Paoli, G., Stokke, H. H., Rocchi, S., Sirevaag, H., Ksienzyk, A. K., Jacobs, J., & Košler, J. (2017). Basement provenance revealed by U–Pb detrital zircon ages: a tale of African and European heritage in Tuscany, Italy. *Lithos*, 277, 376-387.

Papeschi, S., Musumeci, G., & Mazzarini, F. (2017). Heterogeneous brittle-ductile deformation at shallow crustal levels under high thermal conditions: The case of a synkinematic contact aureole in the inner Northern Apennines, southeastern Elba Island, Italy. *Tectonophysics*, 717, 547-564.

Papeschi, S., Musumeci, G., Massonne, H. J., Bartoli, O., & Cesare, B. (2019). Partial melting and strain localization in metapelites at very low-pressure conditions: The Northern Apennines magmatic arc on the Island of Elba, Italy. *Lithos*, 350, 105230.

Papeschi, S., Musumeci, G., Massonne, H. J., Mazzarini, F., Ryan, E. J., & Viola, G. (2020). High-P ($P = 1.5\text{--}1.8$ GPa) blueschist from Elba: Implications for underthrusting and exhumation of continental units in the Northern Apennines. *Journal of Metamorphic Geology*, 38 (5), 495-525.

Parra, T., Vidal, O., & Jolivet, L. (2002). Relation between the intensity of deformation and retrogression in blueschist metapelites of Tinos Island (Greece) evidenced by chlorite–mica local equilibria. *Lithos*, 63(1-2), 41-66.

Passchier, C. W., & Trouw, R. A. (2005). *Microtectonics*. Springer Science & Business Media.

Patacca, E., & Scandone, P. (1985). Struttura geologica dell'Appennino emiliano-romagnolo: ipotesi sismotettoniche. *Atti del Seminario "Progetto Cartografia Geologica"*, Bologna, 22-23 Febbraio 1985, pp. 102–118. Regione Emilia-Romagna, Bologna.

Patacca, E., Sartori, R., & Scandone, P. (1990). Tyrrhenian basin and Apenninic arcs: kinematic relations since late Tortonian times. *Memorie della Società Geologica Italiana*, 45, 425-451.

Patacca, E., Scandone, P., Conti, P., Mancini, S., & Massa, G. (2013). Ligurian-derived olistostrome in the Pseudomacigno Formation of the Stazzema Zone (Alpi Apuane, Italy). Geological implications at regional scale. *Italian Journal of Geosciences*, 132(3), 463-476.

Penniston-Dorland, S. C., Kohn, M. J., & Manning, C. E. (2015). The global range of subduction zone thermal structures from exhumed blueschists and eclogites: Rocks are hotter than models. *Earth and Planetary Science Letters*, 428, 243–254. <https://doi.org/10.1016/j.epsl.2015.07.031>

Pertusati, P. C., Musumeci, G., Bonini, L. & Franceschi, M. (2004). The serie ridotta in southern Tuscany: a cartographic example and consideration on the origin. In: Morini, D. & Bruni, (Eds.) *The 'Regione Toscana' Project of Geological Mapping: Case Histories and Data Acquisition*, 183–185.

Platt, J. P. (1986). Dynamics of orogenic wedges and the uplift of high-pressure metamorphic rocks. *Geological society of America bulletin*, 97(9), 1037-1053.

Plunder, A., Agard, P., Chopin, C., Pourteau, A., & Okay, A. I. (2015). Accretion, underplating and exhumation along a subduction interface: From subduction initiation to continental subduction (Tavşanlı zone, W. Turkey). *Lithos*, 226, 233-254.

Pourteau, A., Bousquet, R., Vidal, O., Plunder, A., Duisterhoeft, E., Candan, O., & Oberhänsli, R. (2014). Multistage growth of Fe–Mg–carpholite and Fe–Mg–chloritoid, from field evidence to thermodynamic modelling. *Contributions to Mineralogy and Petrology*, 168(6), 1090.

Rahl, J. M., Anderson, K. M., Brandon, M. T., & Fassoulas, C. (2005). Raman spectroscopic carbonaceous material thermometry of low-grade metamorphic rocks: Calibration and application to tectonic exhumation in Crete, Greece. *Earth and Planetary Science Letters*, 240(2), 339-354.

Ramsay, J. G., & Huber, M. I. (1987). *The techniques of modern structural geology*. Academic press.

Rau A., & Tongiorgi M. (1974). Geologia dei Monti Pisani a Sud-Est della valle del Guappero. *Memorie della Società Geologica Italiana*, 13, 227-408.

Ricci, C. A. (1972). Geo-petrological features of the metamorphic formation of Tuscany. *Atti della Società Toscana di Scienze Naturali, Memorie, Serie A*, 79, 267-279.

Ricci, C.A., & Serri, G., (1975). Evidenze geochimiche sulla diversa affinità petrogenetica delle rocce basiche comprese nelle serie a facies toscana. *Bollettino della Società Geologica Italiana*, 94, 1187- 1198.

Ring, U., & Layer, P. W. (2003). High-pressure metamorphism in the Aegean, eastern Mediterranean: Underplating and exhumation from the Late Cretaceous until the Miocene to Recent above the retreating Hellenic subduction zone. *Tectonics*, 22(3), 1022.

Rossetti, F., Faccenna, C., Jolivet, L., Funiciello, R., Tecce, F., & Brunet, C. (1999). Syn- versus post-orogenic extension: the case study of Giglio Island (Northern Tyrrhenian Sea, Italy). *Tectonophysics*, 304(1-2), 71-93.

Rossetti, F., Faccenna, C., Goffé, B., Monié, P., Argentieri, A., Funiciello, R., & Mattei, M. (2001a). Alpine structural and metamorphic signature of the Sila Piccola Massif nappe stack (Calabria,

Italy): Insights for the tectonic evolution of the Calabrian Arc. *Tectonics*, 20(1), 112–133.

<https://doi.org/10.1029/2000TC900027>

- Rossetti, F., Faccenna, C., Jolivet, L., Funicello, R., Goffé, B., Tecce, F., & Vidal, O. (2001b). Structural signature and exhumation PTt path of the Gorgona blueschist sequence (Tuscan Archipelago, Italy). *Ofioliti*, 26(2a), 175-186.
- Rossetti, F., Goffé, B., Monié, P., Faccenna, C., & Vignaroli, G. (2004). Alpine orogenic P-T-t-deformation history of the Catena Costiera area and surrounding regions (Calabrian Arc, southern Italy): The nappe edifice of north Calabria revised with insights on the Tyrrhenian-Apennine system formation. *Tectonics*, 23(6).
- Rossetti, F., Balsamo, F., Villa, I. M., Bouybaouenne, M., Faccenna, C., & Funicello, R. (2008). Pliocene–Pleistocene HT–LP metamorphism during multiple granitic intrusions in the southern branch of the Larderello geothermal field (southern Tuscany, Italy). *Journal of the Geological Society*, 165(1), 247-262.
- Rubatto, D., & Hermann, J. (2001). Exhumation as fast as subduction? *Geology*, 29(1), 3-6.
- Rubatto, D., & Hermann, J. (2003). Zircon formation during fluid circulation in eclogites (Monviso, Western Alps): implications for Zr and Hf budget in subduction zones. *Geochimica et Cosmochimica acta*, 67(12), 2173-2187.
- Ryan, E., Papeschi, S., Viola, G., Musumeci, G., Mazzarini, F., Torgersen, E., ... & Ganerød, M. (2021). Syn-orogenic exhumation of high-P units by upward extrusion in an accretionary wedge: Insights from the Eastern Elba nappe stack (Northern Apennines, Italy). *Tectonics*, 40(5), e2020TC006348.

Scambelluri, M., Pettke, T., & Cannà, E. (2015). Fluid-related inclusions in Alpine high-pressure peridotite reveal trace element recycling during subduction-zone dehydration of serpentinized mantle (Cima di Gagnone, Swiss Alps). *Earth and Planetary Science Letters*, 429, 45-59.

Serri, G., Innocenti, F., & Manetti, P. (1993). Geochemical and petrological evidence of the subduction of delaminated Adriatic continental lithosphere in the genesis of the Neogene-Quaternary magmatism of central Italy. *Tectonophysics*, 223(1-2), 117-147.

Signorini, R. (1949). Visione odierna della geologia toscana. *Bollettino della Società Geologica Italiana* 65, 82-90.

Signorini, R. (1966). Il verrucano della Toscana Meridionale. *Atti del Symposium sul Verrucano*, 55-71.

Siivola, J., & Schmid, R. (2007). List of mineral abbreviations. *Metamorphic Rocks: A Classification and Glossary of Terms. Recommendations of the International Union of Geological Sciences Subcommittee on the Systematics of Metamorphic Rocks*, 93-110.

Smith, S. A. F., Holdsworth, R. E., Collettini, C., & Pearce, M. A. (2011). The microstructural character and mechanical significance of fault rocks associated with a continental low-angle normal fault: the Zuccale Fault, Elba Island, Italy. *Geological Society, London, Special Publications*, 359(1), 97-113.

Storti, F. (1995). Tectonics of the Punta Bianca promontory: Insights for the evolution of the Northern Apennines-Northern Tyrrhenian Sea basin. *Tectonics*, 14(4), 832-847.

Tajčmanová, L., Connolly, J. A. D., & Cesare, B. (2009). A thermodynamic model for titanium and ferric iron solution in biotite. *Journal of Metamorphic Geology*, 27(2), 153-165.

Theye, T., Seidel, E., & Vidal, O. (1992). Carpholite, sudoite, and chloritoid in low-grade high-pressure metapelites from Crete and the Peloponnese, Greece. *European Journal of Mineralogy*, 487-508.

Theye, T., Reinhardt, J., Goffé, B., Jolivet, L., & Brunet, C. (1997). Ferro-and magnesiocarpholite from the Monte Argentario (Italy): First evidence for high-pressure metamorphism of the metasedimentary Verrucano sequence, and significance for PT path reconstruction. *European Journal of Mineralogy*, 859-874.

Tobisch, O. T., & Paterson, S. R. (1988). Analysis and interpretation of composite foliations in areas of progressive deformation. *Journal of Structural Geology*, 10(7), 745-754.

Trigila R. (1966). Studio geo-petrografico dell'edificio vulcanico di M. Calvo (Farnese-Viterbo). *Periodico di Mineralogia*, 25, 1023-1102

Varekamp, J. C. (1980). The geology of the Vulsinian area, Lazio, Italy. *Bulletin Volcanologique*, 43(3), 489-503.

Verrucchi, C., Pandeli, E., Minissale, A., Andreotti, P., & Paolieri, M. (1994). New data for the geochemical characterization of the Tuscan Paleozoic sequences (Northern Apennines, Italy). *Mem. Soc. Geol. It*, 48, 655-666.

Vidal, O., & Parra, T. (2000). Exhumation paths of high-pressure metapelites obtained from local equilibria for chlorite–phengite assemblages. *Geological Journal*, 35(3-4), 139-161.

Vidal, O., Goffé, B., Bousquet, R., & Parra, T. (1999). Calibration and testing of an empirical chloritoid-chlorite Mg-Fe exchange thermometer and thermodynamic data for daphnite. *Journal of Metamorphic geology*, 17, 25-40.

Vidal, O., de Andrade, V., Lewin, E., Munoz, M., Parra, T., & Pascarelli, S. (2006). P–T-deformation- $\text{Fe}^{3+}/\text{Fe}^{2+}$ mapping at the thin section scale and comparison with XANES mapping: application to a garnet-bearing metapelite from the Sambagawa metamorphic belt (Japan). *Journal of Metamorphic Geology*, 24(7), 669-683.

Vignaroli, G., Faccenna, C., Rossetti, F., & Jolivet, L. (2009). Insights from the Apennines metamorphic complexes and their bearing on the kinematics evolution of the orogen. *Geological Society, London, Special Publications*, 311(1), 235-256.

Vitale Brovarone, A., & Herwartz, D. (2013). Timing of HP metamorphism in the Schistes Lustrés of Alpine Corsica: New Lu–Hf garnet and lawsonite ages. *Lithos*, 172, 175-191.

Vitale, S., Fedele, L., Tramparulo, F. D. A., Ciarcia, S., Mazzoli, S., & Novellino, A. (2013). Structural and petrological analyses of the Frido Unit (southern Italy): New insights into the

early tectonic evolution of the southern Apennines–Calabrian Arc system. *Lithos*, 168, 219-235.

Warren C J. 2012. Up the down escalator: The exhumation of (ultra)-high pressure terranes during on-going subduction. *Solid Earth*, 4, 75–92, <https://doi.org/10.5194/se-4-75-2013>, 2013.

White, R. W., Powell, R., Holland, T. J. B., Johnson, T. E., & Green, E. C. R. (2014). New mineral activity–composition relations for thermodynamic calculations in metapelitic systems. *Journal of Metamorphic Geology*, 32(3), 261-286.

Worley, B., Powell, R., & Wilson, C. J. (1997). Crenulation cleavage formation: Evolving diffusion, deformation and equilibration mechanisms with increasing metamorphic grade. *Journal of Structural Geology*, 19(8), 1121-1135.

Xie, X., Byerly, G. R., & Ferrell Jr, R. E. (1997). Ilb trioctahedral chlorite from the Barberton greenstone belt: crystal structure and rock composition constraints with implications to geothermometry. *Contributions to Mineralogy and Petrology*, 126(3), 275-291.

Yamato, P., Agard, P., Burov, E., Le Pourhiet, L., Jolivet, L., & Tiberi, C. (2007). Burial and exhumation in a subduction wedge: Mutual constraints from thermomechanical modeling and natural P-T-t data (Schistes Lustrés, western Alps). *Journal of Geophysical Research: Solid Earth*, 112(B7).

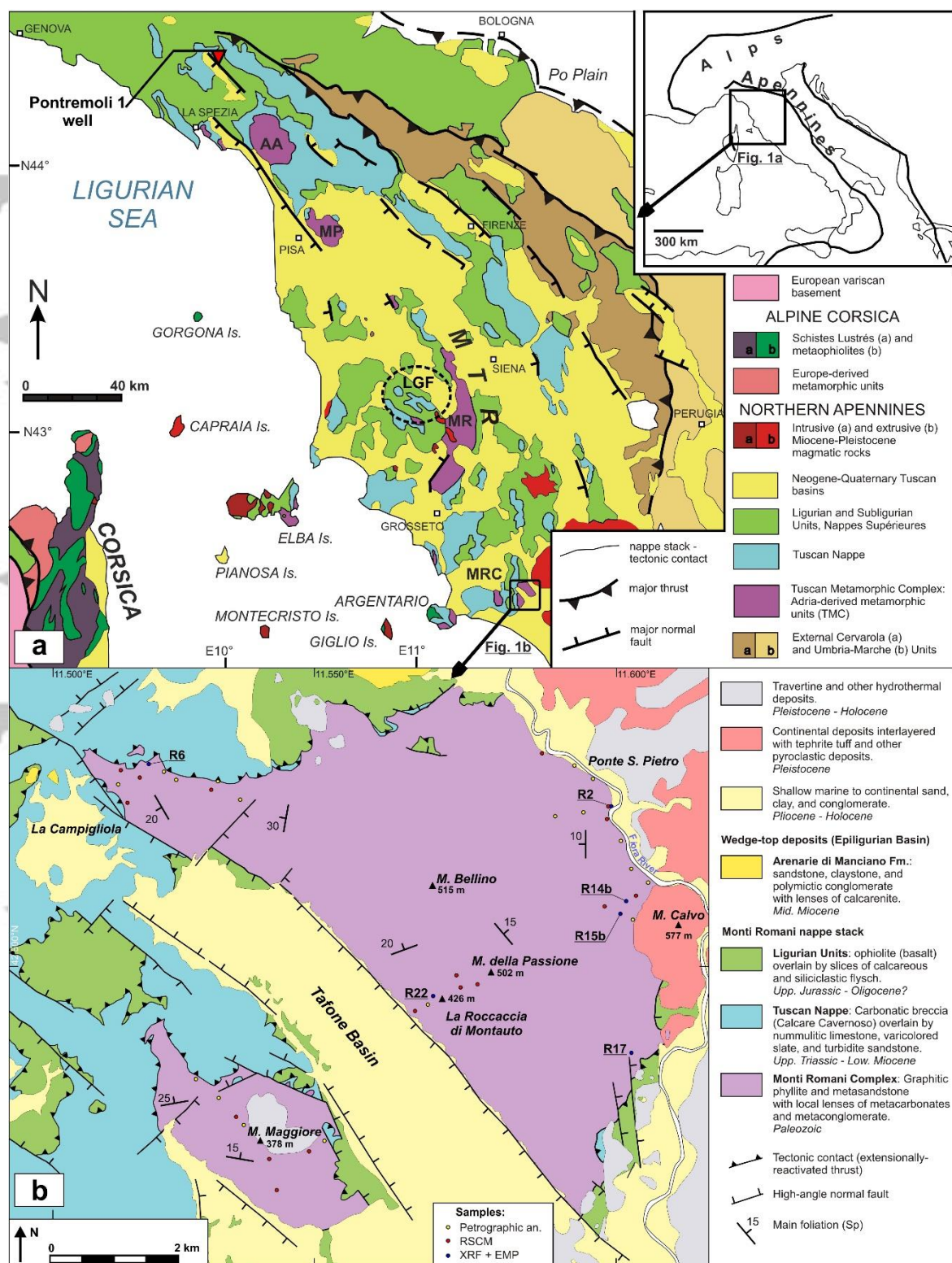


Figure 1 – Tectonic sketch map of (a) the Northern Apennines – Alpine Corsica orogenic system (modified and readapted after Bonini et al., 2014) and (b) the Monti Romani Complex (modified and re-adapted after Moretti, Meletti, & Ottria, 1990), with indication of the studied samples (colored dots). Yellow dots indicate samples used only for petrographic analyses, while red dots and blue dots mark samples that we selected for RSCM thermometry and pseudosection modelling, respectively. AA: Alpi Apuane; LGF: Larderello Geothermal Field; MP: Monti Pisani; MR: Monticiano–Roccastrada; MTR: Mid-Tuscan Ridge.

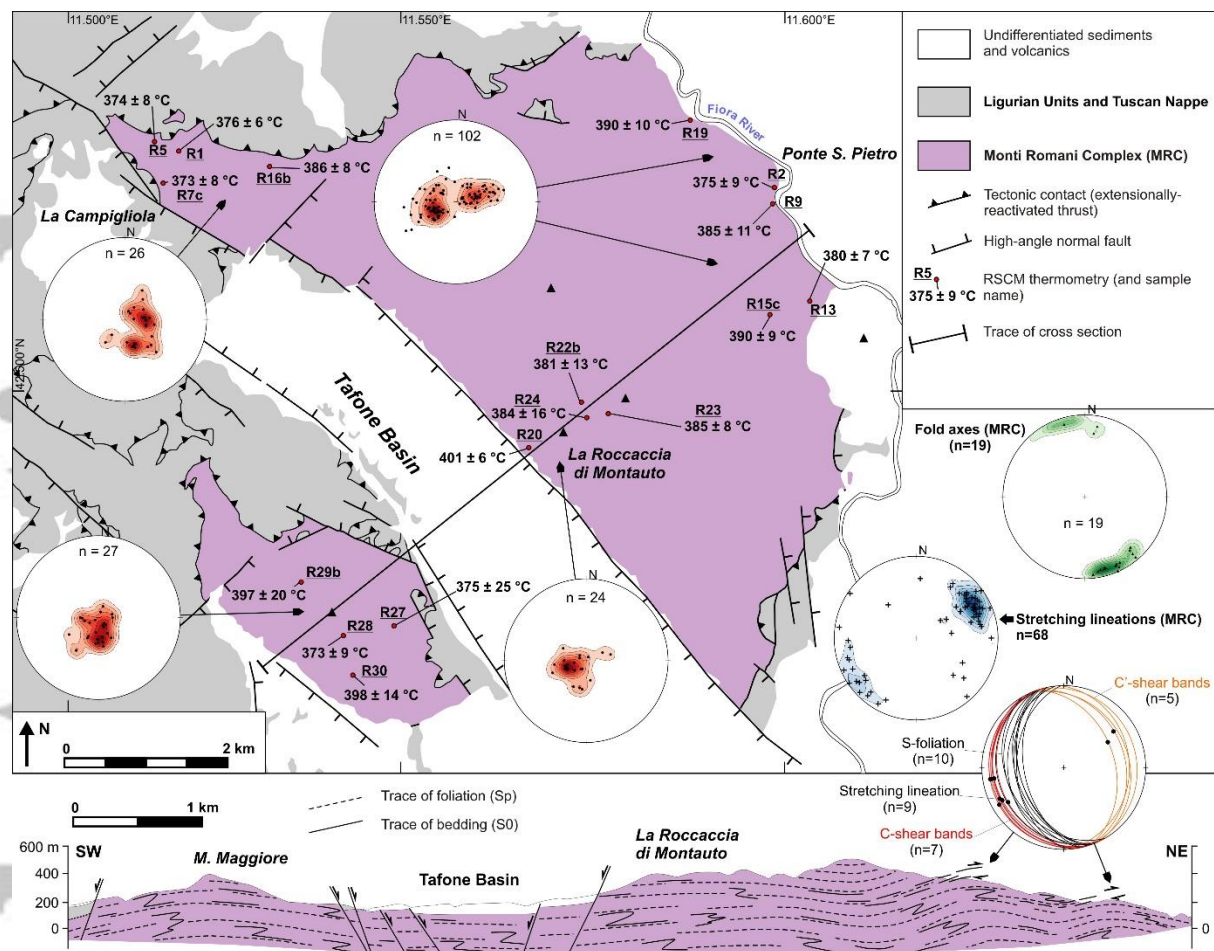


Figure 2 – Geological sketch map of the Monti Romani Complex, showing the main tectonic lineaments. Stereographic projections (equal area, lower hemisphere) highlight the distribution of poles to S_p foliation (red contours), fold axes (green contours), stretching lineations (blue contours) and C-type shear bands. The SW – NE oriented geological cross section presents the attitude of S_p and the geometry of mesoscale folds and shear zones within the Monti Romani Complex. The results of the RSCM thermometry are also shown. Note that the cross section is enlarged with respect to its trace on the map.

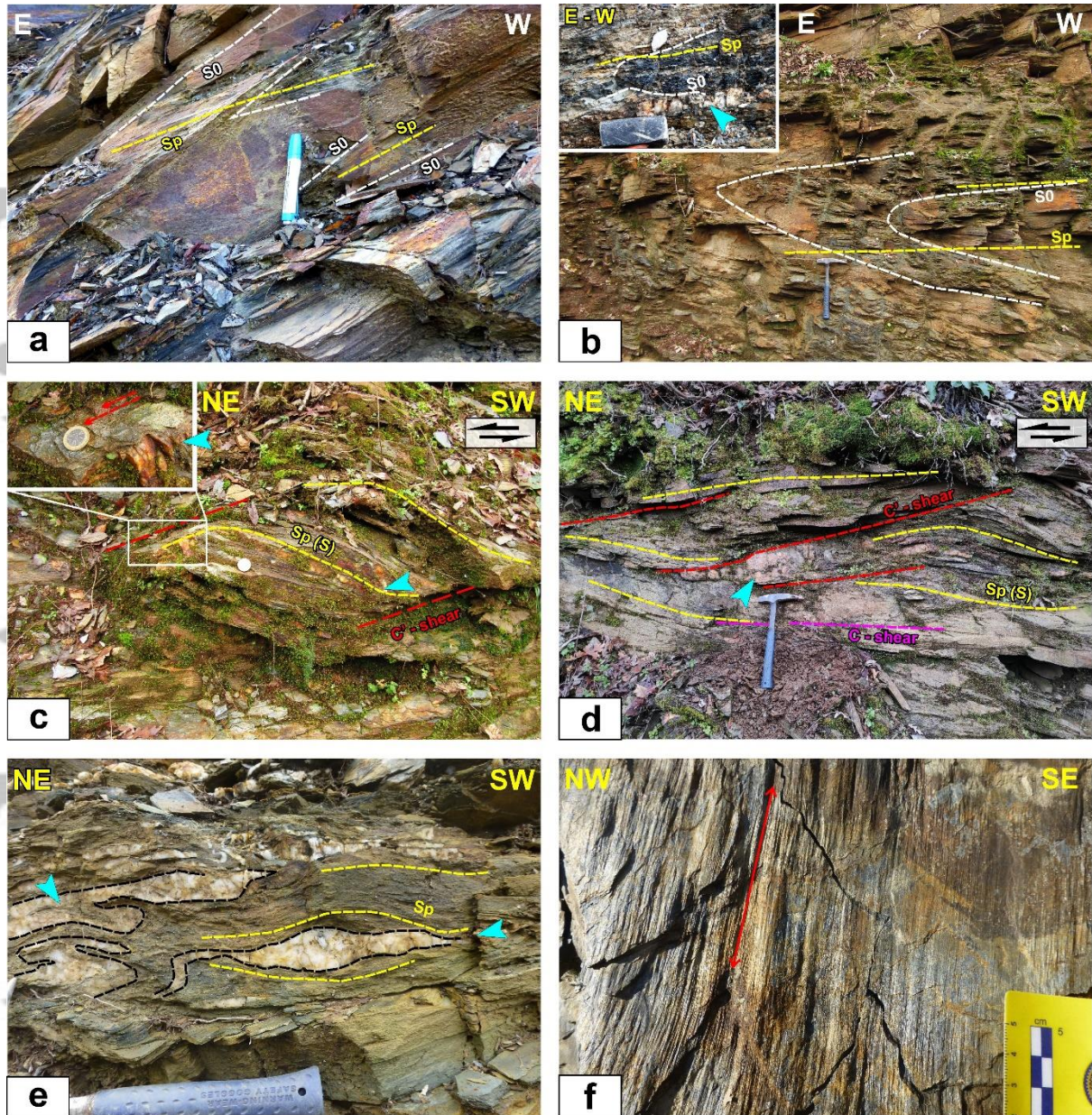


Figure 3 – Mesoscale structures. (a) Relationships between bedding (S_0) and slaty cleavage foliation (S_p) in metasandstone – phyllite layering. (b) Examples of recumbent, NE-verging folds with S_p axial plane foliation. Note the relationships with the S_0 and the refraction of cleavage close to fold hinges. (c) NE-dipping C' shear bands affecting the metamorphic foliation and intrafoliar quartz veins. The inset shows the stretching lineations developed on a shear band. (d) Top-to-the-NE C - and C' -type shear bands that crosscut a sigmoidal S -foliation (S_p). Note the quartz vein boudinage along a shear band. (e) Syn-tectonic quartz veins that are asymmetrically boudinated along the S_p . (f) Intersection lineation (red arrowed line) defined by tightly spaced fold hinges refolding the S_p . The fold axes are sub-parallel to L_p . S_0 : white dashed line. S_p : yellow dashed line. C' -shears: red dashed lines, C -shear: violet dashed lines. Quartz veins are marked by cyan arrows.

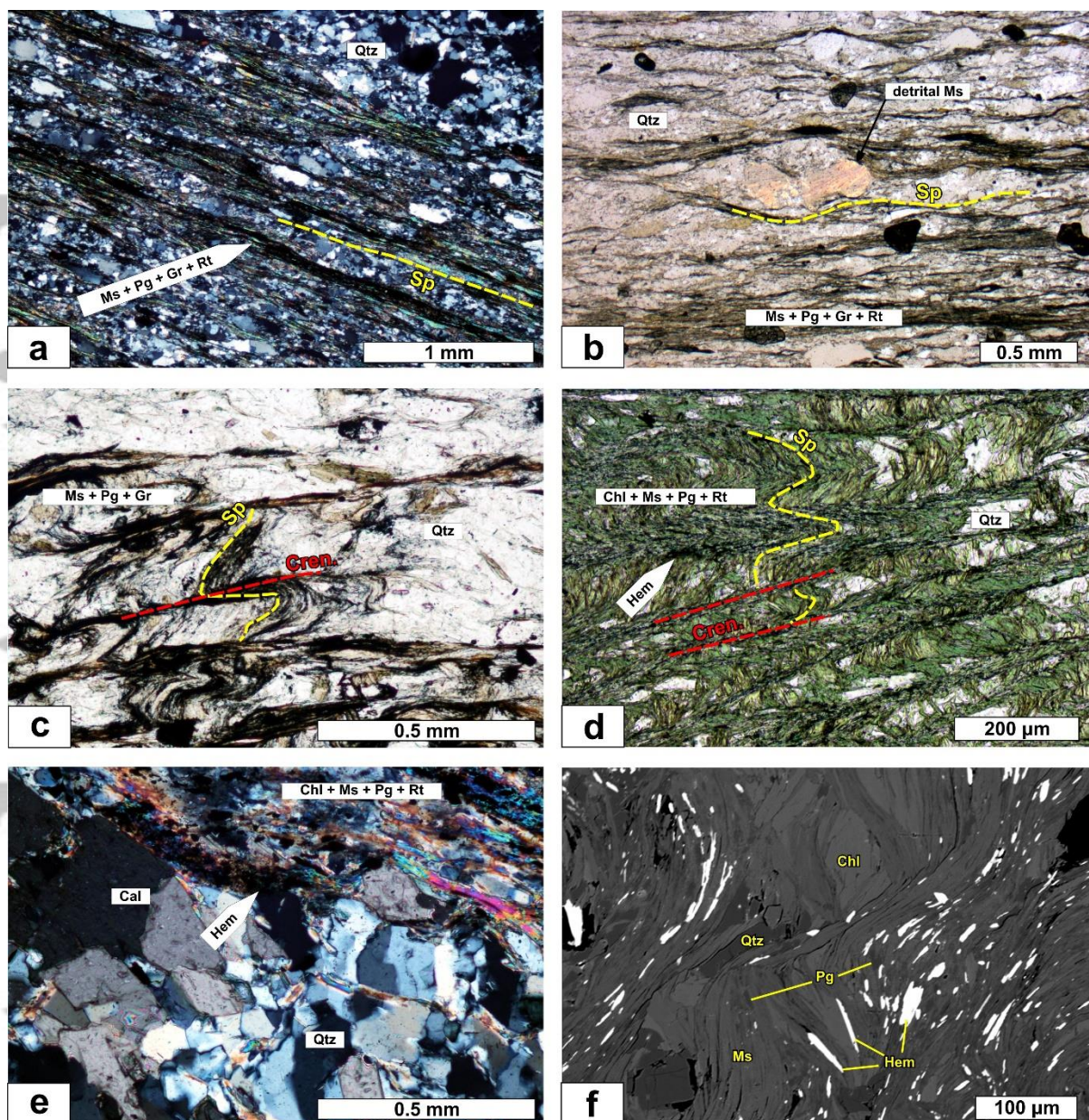


Figure 4 – Microstructures of (a-b-c) graphite- and (d-e-f) chlorite-bearing samples: (a) Continuous, anastomosing cleavage foliation (S_p) defined by white mica- and quartz-rich domains (XPL – Crossed Polarized Light). (b) Detrital white mica grain and quartz-rich domains surrounded by S_p cleavage domains, developed in mica + graphite-rich levels (PPL – Plane Polarized Light). (c) Crenulation cleavage, defined by spaced graphite-rich layers (Cren), that affects the S_p foliation defined by white mica and graphite (PPL). (d) Crenulated S_p foliation made of chlorite + white mica + quartz + hematite. (PPL). (e) Quartz-rich layering containing coarse-grained calcite grains (XPL). (f) Back Scattered Electrons (BSE) image detailing the crenulated domains showing the coexistence of chlorite, muscovite, paragonite, quartz, and hematite. Mineral abbreviations after Siivola & Schmidt (2007).

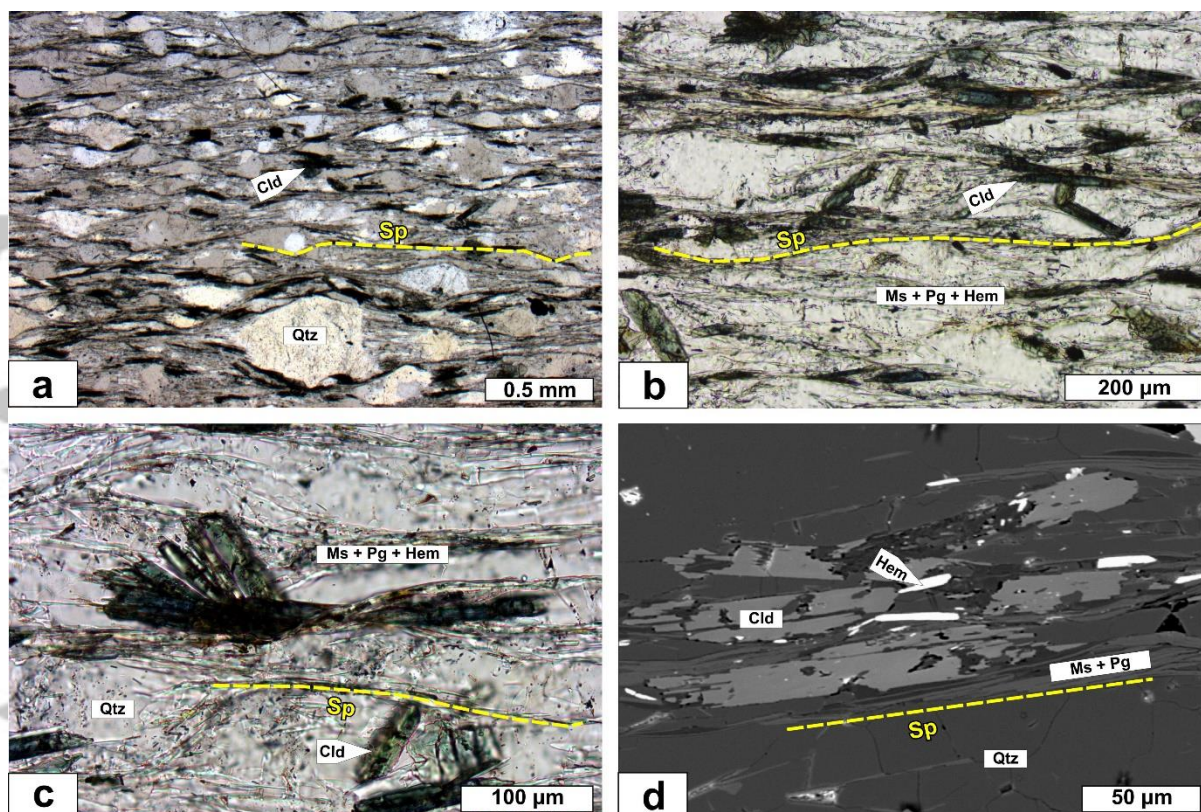


Figure 5 – Microstructures of the chloritoid-bearing samples (R6 and R17). (a) Disjunctive cleavage domains, defined by phyllosilicate + hematite-rich layers anastomosing around quartz grains. Chloritoid (Cld) grains are visible along the S_p foliation (sample R6; PPL). (b) Detail of (a) showing chloritoid grains growing parallel and transverse to the S_p (PPL). (c) Chloritoid grains with decussate microstructure overgrowing the S_p foliation (Sample R17; PPL). (d) BSE image showing chloritoid grains, associated with hematite, muscovite, and paragonite (sample R17). Mineral abbreviations after Siivola & Schmidt (2007).

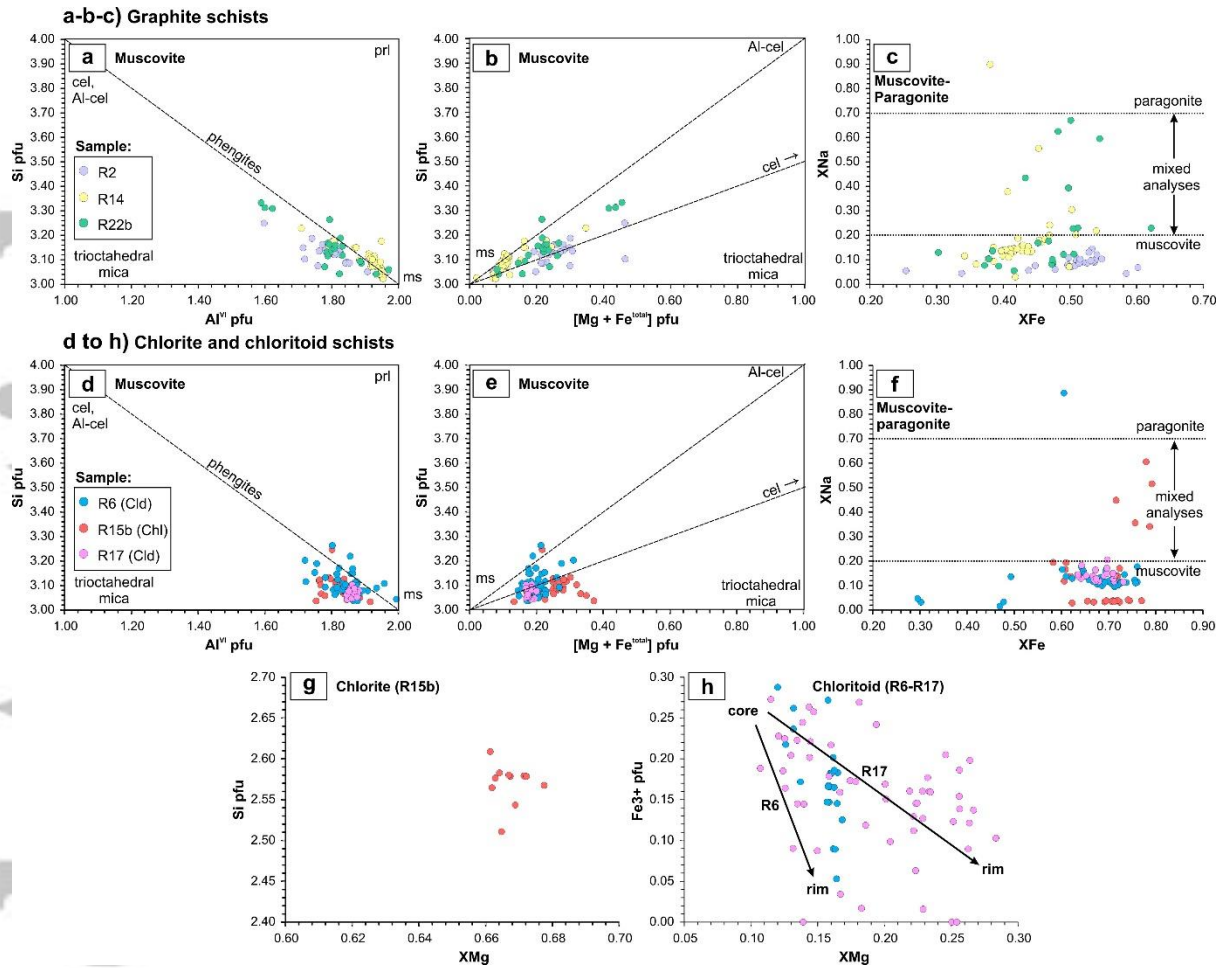


Figure 6 – Mineral chemistry of graphite (a-b-c) and chlorite-chloritoid (d-e-f-g-h) schists. Compositional variability of white mica shown in the Al^{VI} pfu – Si pfu (a-d), $[Mg + Fe^{total}]$ pfu – Si pfu (b-e), and $XFe = [Fe/(Mg + Fe^{total})] - XNa = [Na/(Na + K)]$ plots (c-f). Note the scatter towards the trioctahedral mica component, likely indicating the presence of Fe^{3+} . (g) XMg – Si pfu composition of chlorite in sample R15b. (h) XMg = $[Mg/(Mg + Fe^{total})] - Fe^{3+}$ pfu composition of chloritoid in samples R6 and R17. Chloritoid is Fe-rich in the core and Mg-rich in the rim. Mineral and endmember abbreviations after Siivola & Schmidt (2007).

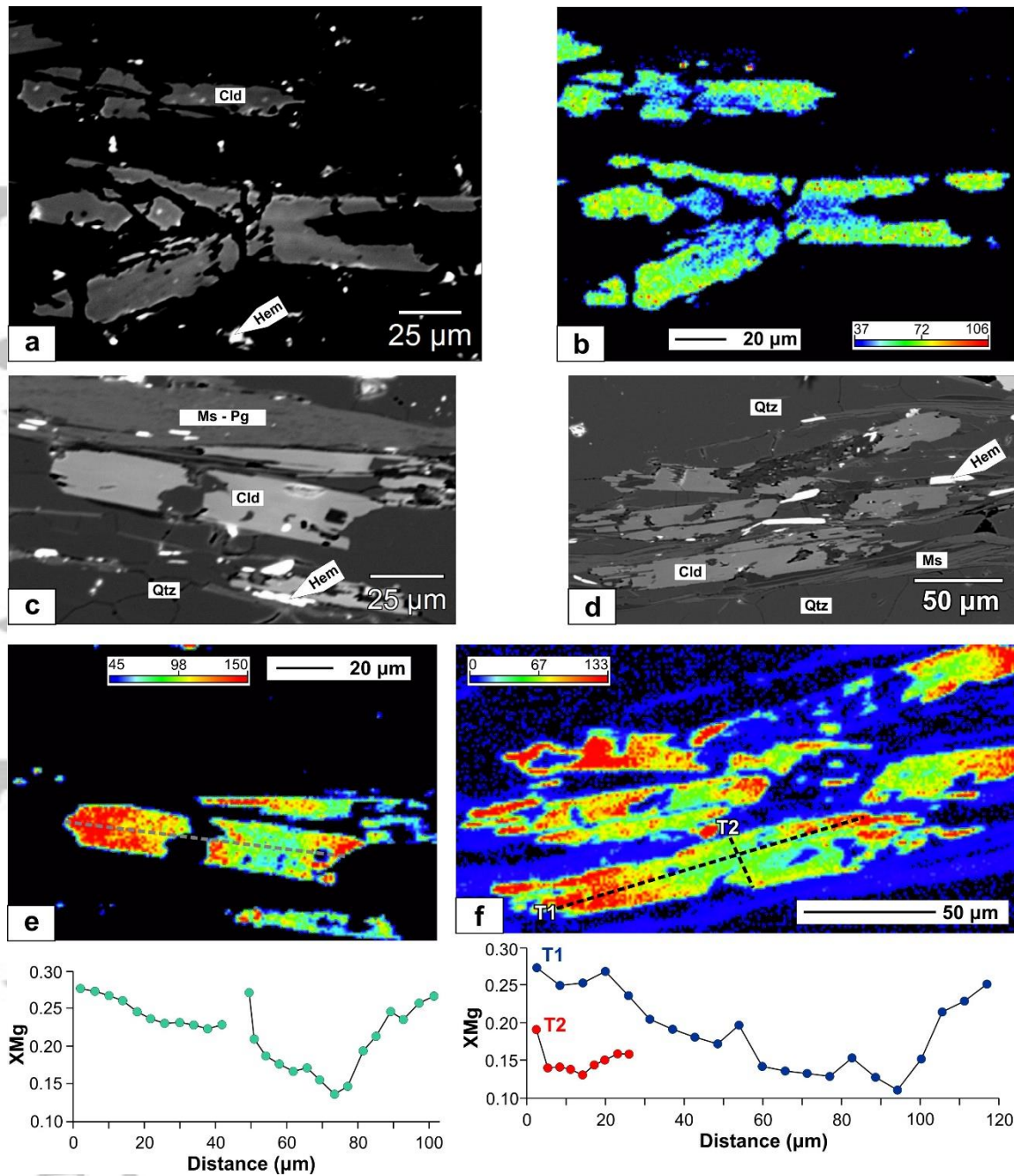


Figure 7 – Mineral chemistry and X-ray maps of chloritoid-bearing samples (R6 and R17). (a) BSE Image and (b) qualitative compositional X-ray map for Mg of prismatic chloritoid grains in the chloritoid schist R6. (c-d) BSE images highlighting the location of (e-f) X-ray maps for Mg intensity in the chloritoid schist R17. T0, T1, and T2 (and corresponding dashed lines) highlight the location of transects of spot analyses across chloritoid grains. The scatter graphs below show the composition of chloritoid along transects, in terms of XMg, highlighting the strong zonation from the Fe-rich core to the Mg-rich rim.

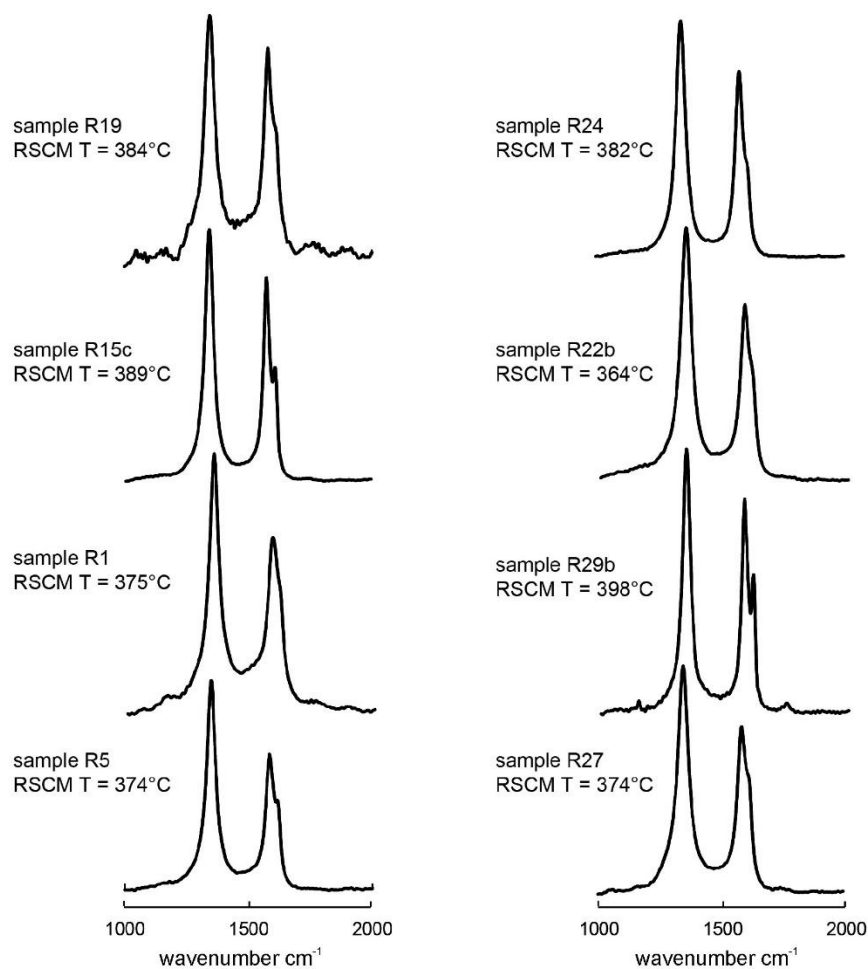


Figure 8 – Representative Raman spectra on carbonaceous material and related RSCM temperatures of selected samples.

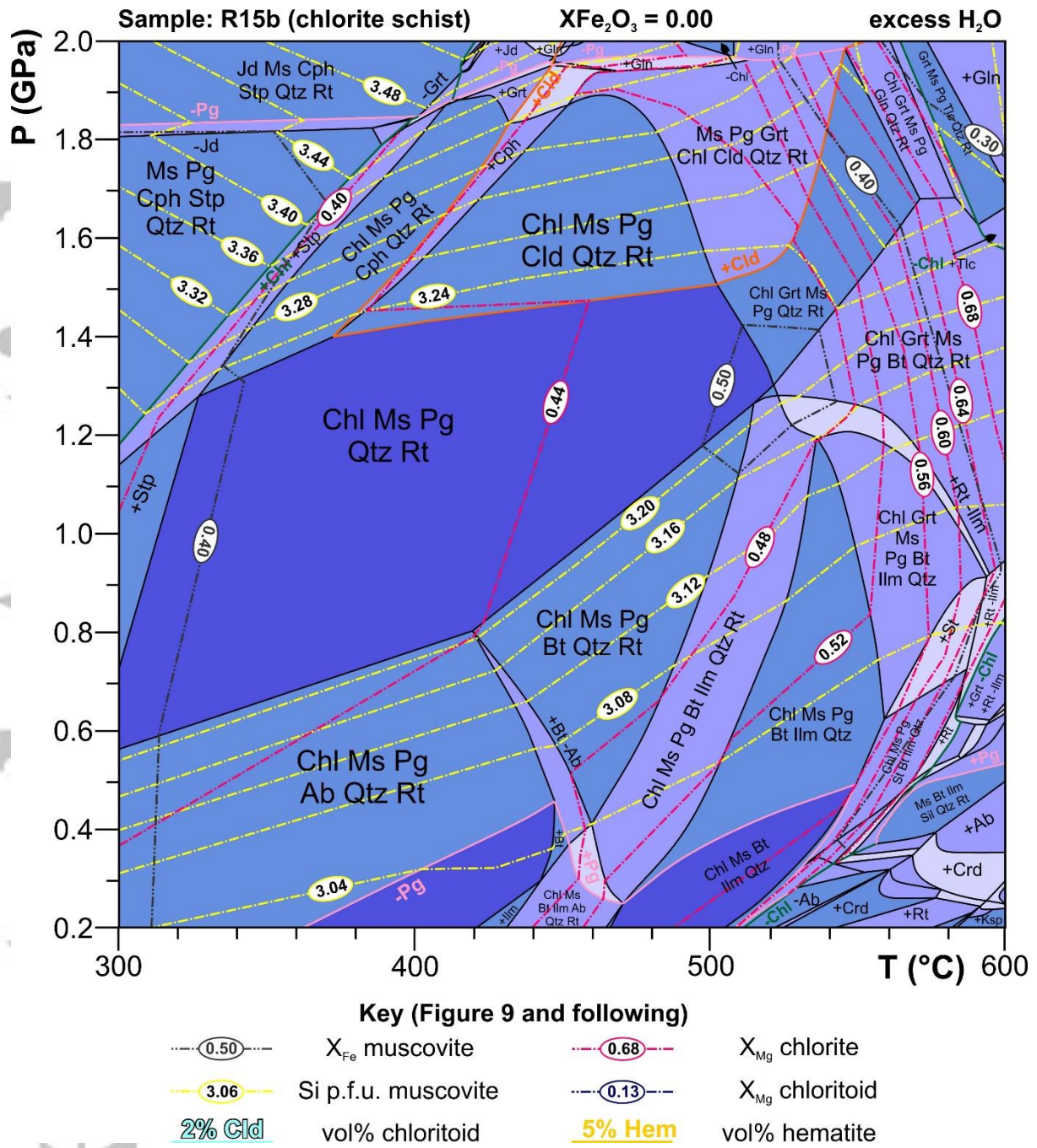


Figure 9 – P–T pseudosection of the chlorite schist R15b (bulk in Table 3; $X_{Fe_2O_3} = 0$).

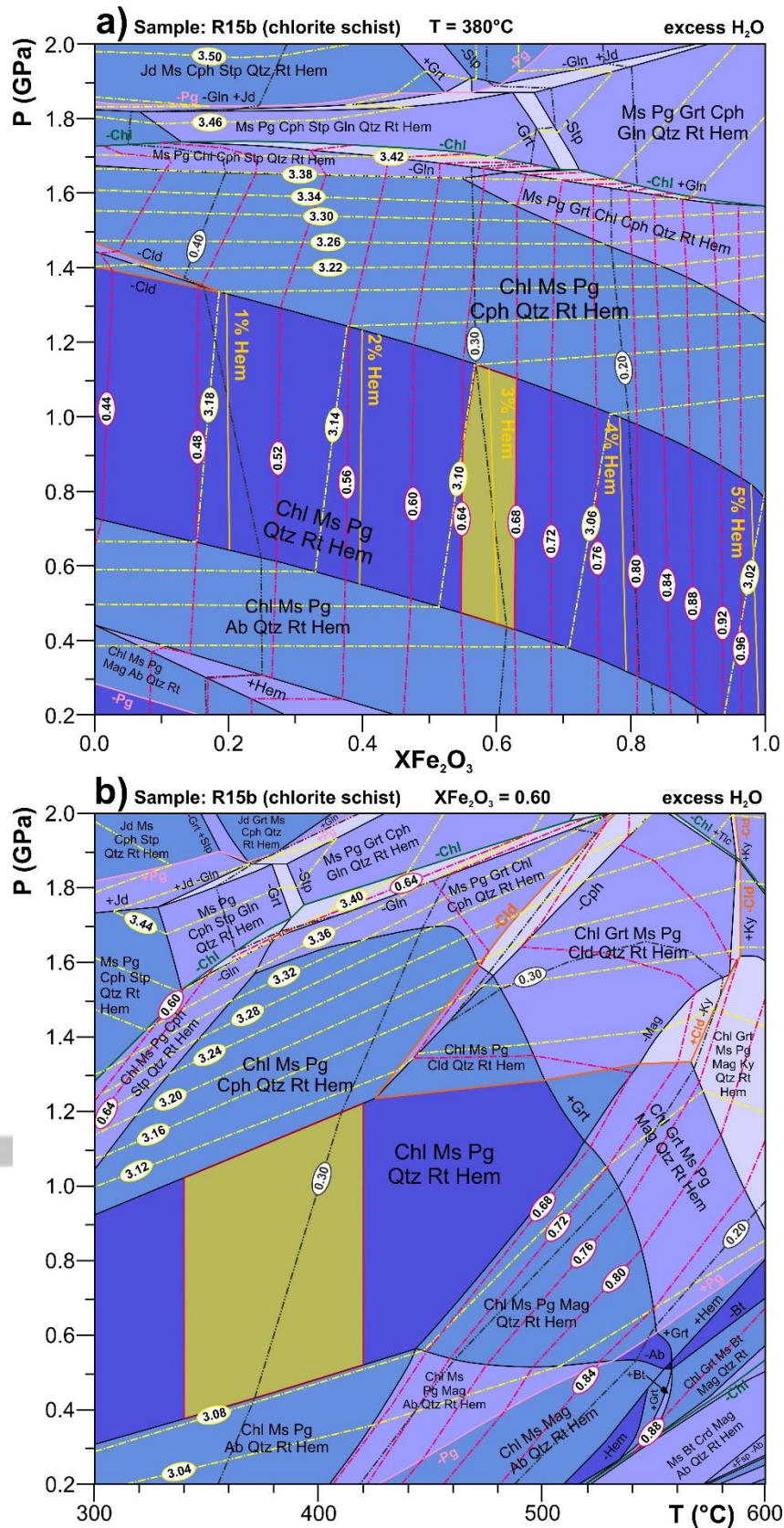


Figure 10 – Pseudosections of the chlorite schist R15b. (a) P–XFe₂O₃ pseudosection calculated for T = 380 °C. Note that hematite mode = 0 for XFe₂O₃ = 0. (b) P–T pseudosection calculated with XFe₂O₃ = 0.6. The yellow field highlights the best fit for the observed parageneses and mineral chemistry.

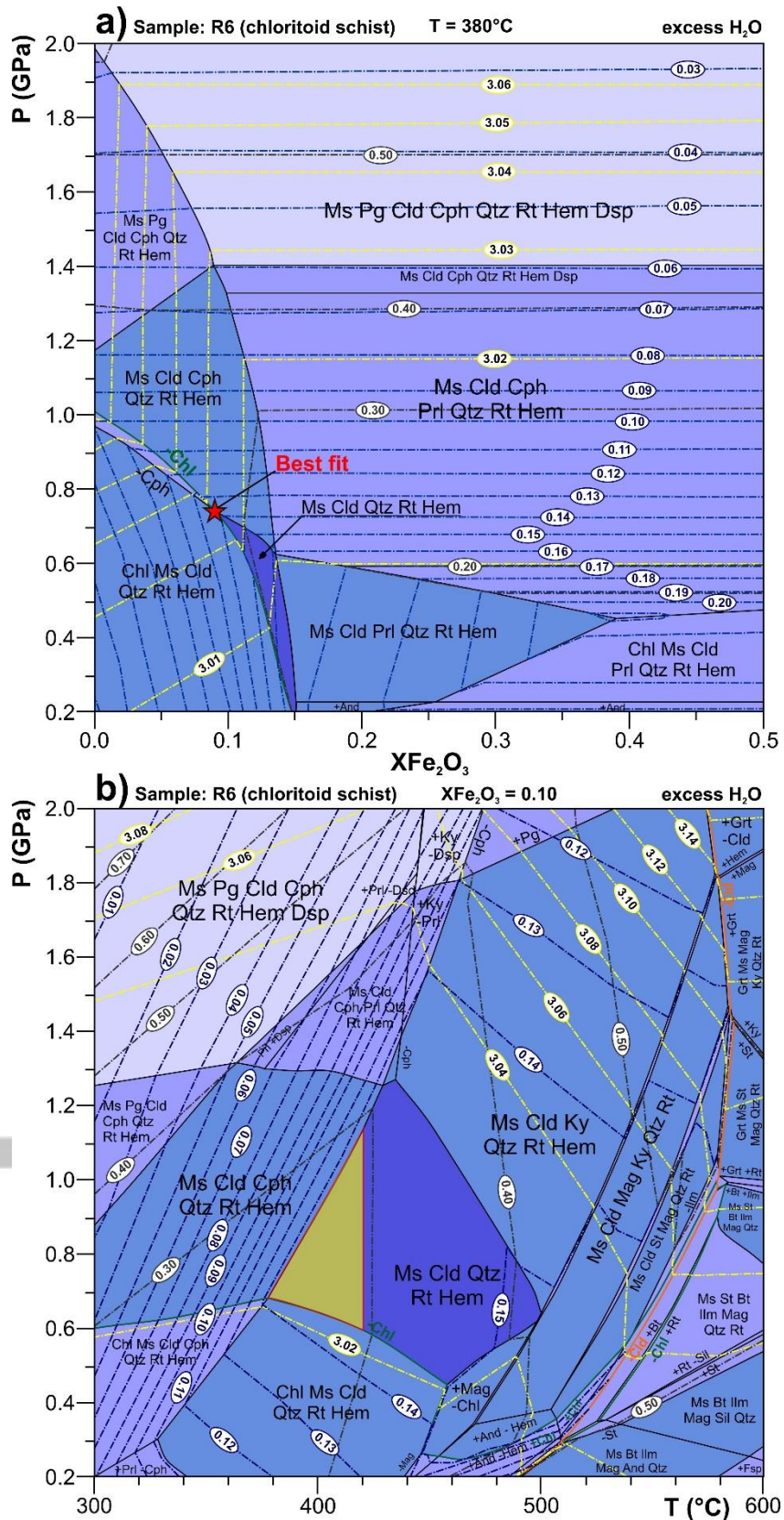


Figure 12 – (a) P – XFe_2O_3 pseudosection of the chloritoid schist R6 calculated for a sectioning value of $T = 380^{\circ}\text{C}$. (b) P – T pseudosection for the chloritoid schist R6 calculated for $\text{XFe}_2\text{O}_3 = 0.1$.

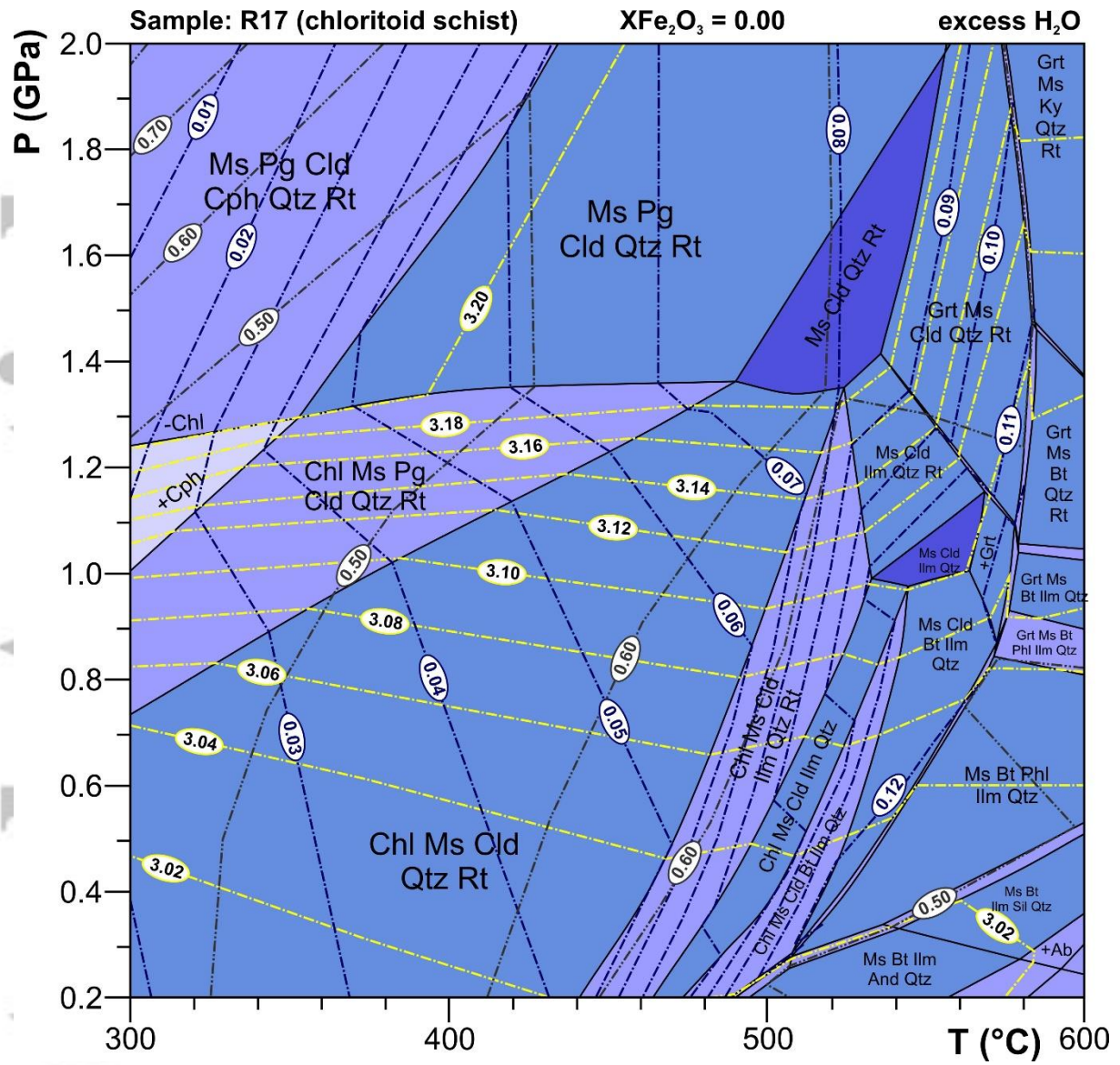


Figure 13 – P–T pseudosection of the chloritoid schist R17 (bulk in Table 3; $X\text{Fe}_2\text{O}_3 = 0$).

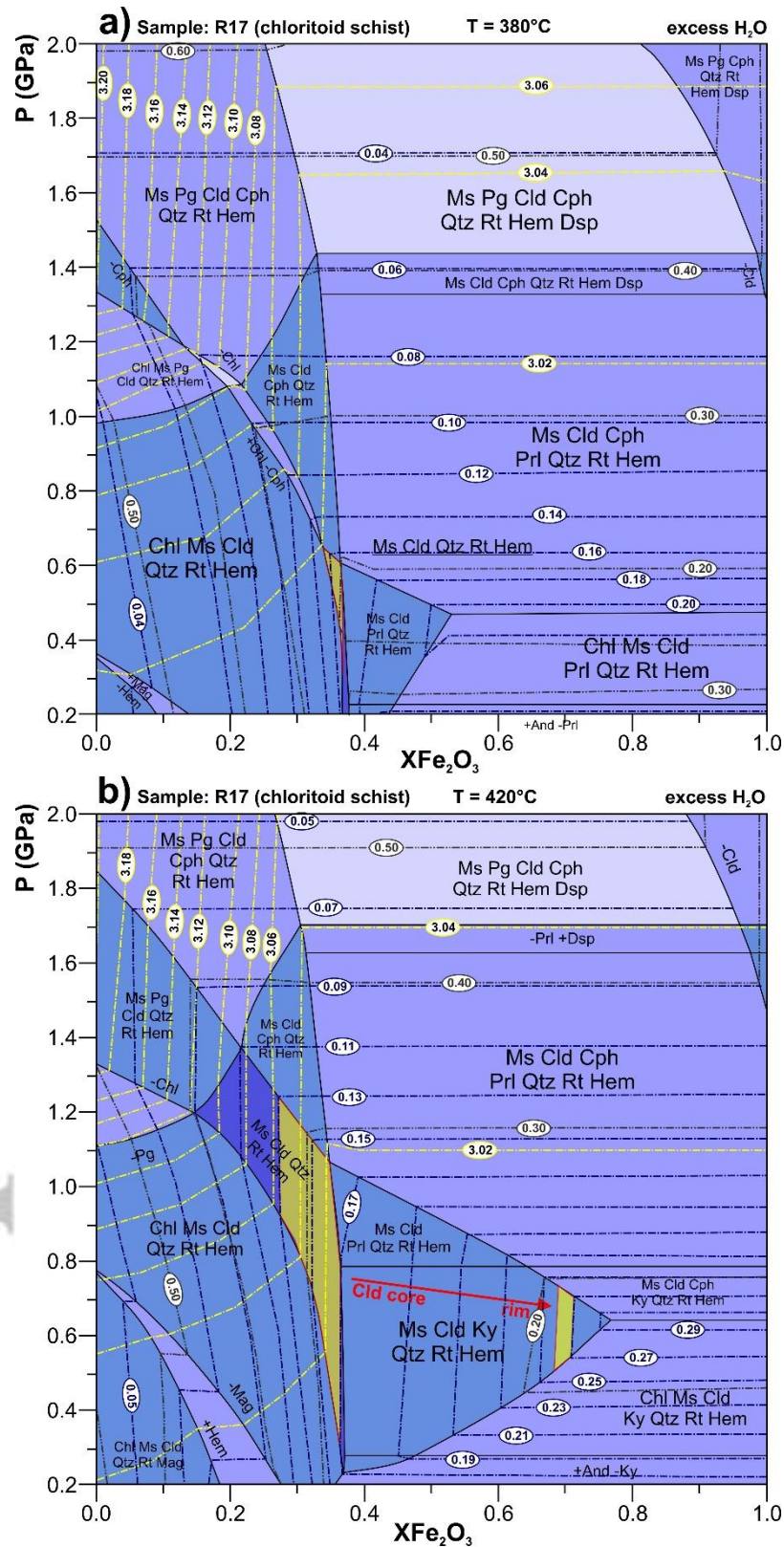


Figure 14 – P–XFe₂O₃ pseudosections of the chloritoid schist R17 calculated at (a) T = 380 °C and (b) T = 420 °C. In the scenario shown in (b) the chloritoid core is stable for XFe₂O₃ = 0.3–0.4 and the rim for XFe₂O₃ up to 0.7. See text for a detailed discussion.

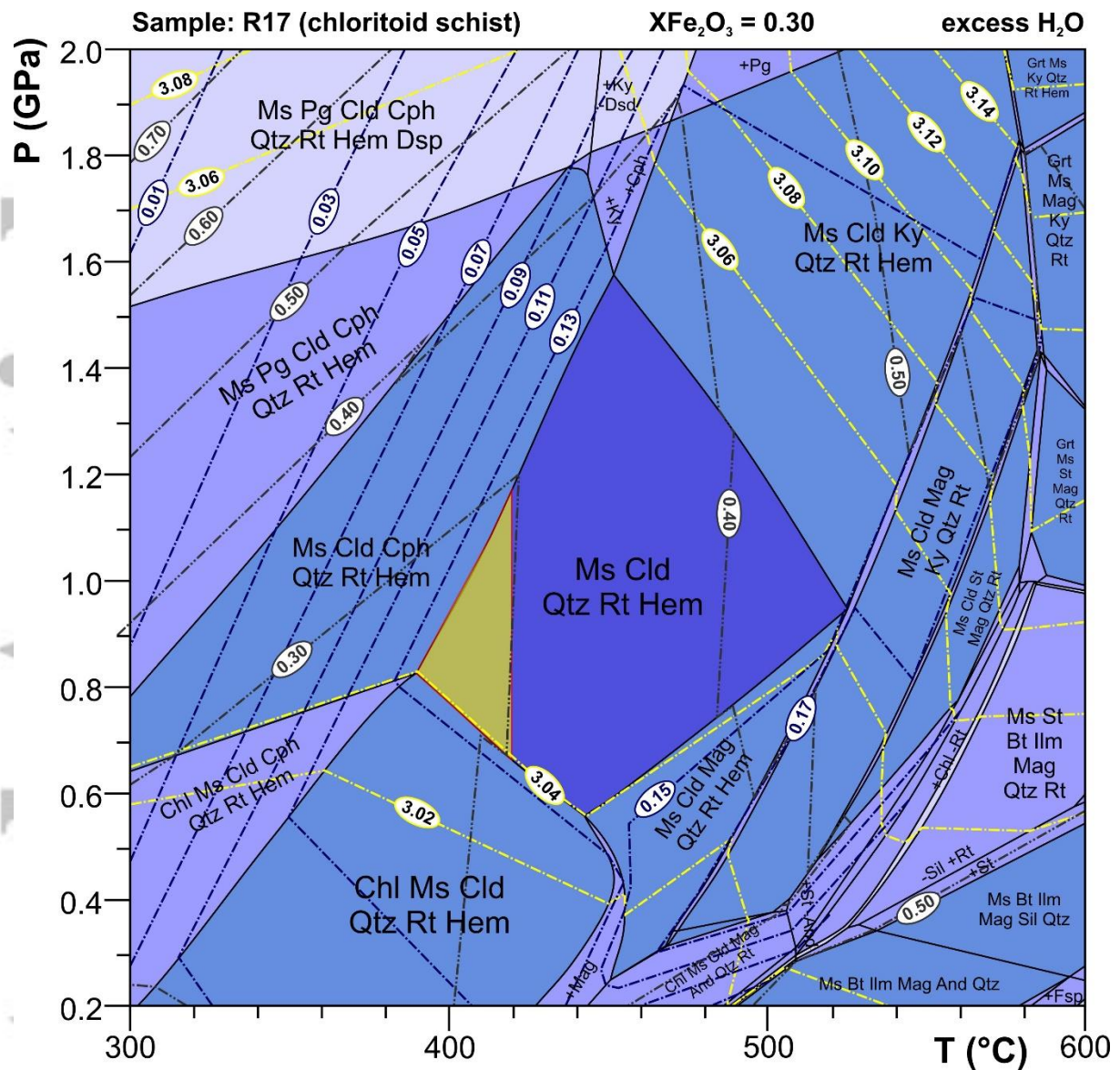


Figure 15 – P–T pseudosection of the chloritoid schist R17 calculated for $X_{Fe_2O_3} = 0.3$.

Table 1 – Representative microprobe analyses of white mica and paragonite, recalculated on 11 oxygen basis. Note that FeO has been considered entirely as divalent.

Analysis	Graphite-bearing						Chlorite-bear.			Chloritoid-bearing					
	R2		detr.	R14b		detr.	R22b		R15b			R6		R17	
	metamorphic			metamorphic			metamorphic		metamorphic		metamorphic		metamorphic		
	43	66	52	24	3	29	42	59	10	30	1	30	4-3	4-43	4-45
SiO ₂	46.65	45.06	47.11	47.45	46.05	47.94	46.81	44.53	46.62	45.03	46.62	47.17	48.80	44.69	45.36
TiO ₂	0.13	0.18	0.35	0.10	0.00	0.06	0.46	0.67	0.11	0.13	0.10	0.11	0.18	0.09	0.10
Al ₂ O ₃	33.01	34.26	28.89	34.79	38.78	31.24	34.56	32.96	34.29	33.90	37.59	33.95	40.13	35.05	35.05
FeOtot	1.99	1.99	2.04	1.17	0.15	2.58	1.21	3.04	3.13	3.31	1.85	2.64	0.37	2.43	2.25
MnO	0.00	0.02	0.00	0.01	0.00	0.03	0.00	0.00	0.01	0.00	0.00	0.00	0.00	0.02	0.00
MgO	1.37	0.98	3.36	0.98	0.13	2.01	1.09	1.21	0.74	0.89	0.33	0.69	0.14	0.55	0.46
CaO	0.00	0.01	0.01	0.02	0.00	0.01	0.00	0.00	0.01	0.04	0.05	0.00	0.24	0.02	0.00
BaO	0.13	0.14	0.44	0.22	0.01	0.16	0.31	0.09	1.18	1.07	0.11	0.28	0.00	0.31	0.36
Na ₂ O	0.53	0.96	0.39	0.78	5.94	0.21	0.98	0.30	0.19	0.24	4.42	0.79	6.19	0.88	0.78
K ₂ O	9.77	8.60	10.06	9.10	1.02	10.42	9.42	9.83	8.79	9.12	4.39	9.82	1.21	9.52	9.08
Total	93.58	92.60	92.64	94.62	92.08	94.67	94.84	92.62	95.08	93.72	95.45	95.46	97.24	93.53	93.44
Si	3.16	3.09	3.25	3.15	3.03	3.23	3.12	3.08	3.13	3.08	3.03	3.15	3.04	3.05	3.08
Al ^{IV}	0.84	0.91	0.75	0.85	0.97	0.77	0.88	0.92	0.87	0.92	0.97	0.85	0.96	0.95	0.92
Al ^{VI}	1.80	1.85	1.60	1.87	2.03	1.71	1.83	1.76	1.79	1.81	1.92	1.82	1.99	1.86	1.88
Ti	0.01	0.01	0.02	0.00	0.00	0.00	0.02	0.03	0.01	0.01	0.01	0.01	0.01	0.00	0.01
Fe ²⁺	0.11	0.11	0.12	0.06	0.01	0.15	0.07	0.18	0.18	0.19	0.10	0.15	0.02	0.14	0.13
Mn	0.00	0.00	0.00	0.00	0.00	0.00	0.00	0.00	0.00	0.00	0.00	0.00	0.00	0.00	0.00
Mg	0.14	0.10	0.35	0.10	0.01	0.20	0.11	0.12	0.07	0.09	0.03	0.07	0.01	0.06	0.05
Ca	0.00	0.00	0.00	0.00	0.00	0.00	0.00	0.00	0.00	0.00	0.00	0.00	0.02	0.00	0.00
Ba	0.00	0.00	0.01	0.01	0.00	0.00	0.01	0.00	0.03	0.03	0.00	0.01	0.00	0.01	0.01
Na	0.07	0.13	0.05	0.10	0.76	0.03	0.13	0.04	0.03	0.03	0.56	0.10	0.75	0.11	0.10
K	0.84	0.75	0.88	0.77	0.09	0.90	0.80	0.87	0.75	0.80	0.33	0.84	0.10	0.83	0.79

Table 2 – Representative microprobe analyses of chlorite (14 Oxygen basis) and chloritoid (12 Oxygen basis). Fe is considered as divalent in chlorite, and recalculated as Fe²⁺ and Fe³⁺ in chloritoid assuming a cation sum of 8 and no vacancies. Temperature estimates using empirical chlorite geothermometers are also shown. Geothermometers: KM: Kranidiotis & McLean (1997); C: Cathelineau (1988); J: Jowett (1991); X: Xie et al., 1997.

	Chlorite				Chloritoid										
	R15b				R6(core)		R6(rim)		R17(core)			R17(rim)			
Analysis	11	23	26	35	2	17	51	4-12	t-8	t-11	t-14	t-1	t-41	t-44	t-46
SiO ₂	25.68	24.96	24.50	25.45	23.11	23.39	23.84	23.64	23.42	24.74	23.44	24.87	24.15	24.28	24.22
TiO ₂	0.03	0.02	0.01	0.03	0.00	0.28	0.04	0.01	0.06	0.04	0.04	0.00	0.03	0.00	0.02
Al ₂ O ₃	23.92	23.54	23.60	23.29	40.22	39.64	40.89	40.08	40.47	40.08	40.04	41.64	40.93	40.97	41.00
FeOtot	18.10	18.12	18.34	18.01	26.10	26.42	26.07	26.17	25.20	24.67	26.81	22.20	22.38	22.64	23.31
MnO	0.11	0.08	0.09	0.04	0.11	0.06	0.07	0.08	0.23	0.24	0.16	0.37	0.30	0.34	0.36
MgO	20.37	20.53	20.40	20.72	2.22	2.24	2.43	2.35	3.43	2.80	2.26	4.51	4.63	4.33	3.94
CaO	0.01	0.00	0.00	0.00	0.00	0.02	0.01	0.00	0.00	0.01	0.00	0.00	0.00	0.00	0.00
BaO	0.00	0.01	0.00	0.01	0.00	0.00	0.03	0.00	0.00	0.00	0.03	0.00	0.01	0.03	0.02
Na ₂ O	0.07	0.00	0.01	0.00	0.00	0.01	0.00	0.00	0.00	0.00	0.01	0.03	0.01	0.01	0.00
K ₂ O	0.09	0.01	0.02	0.07	0.02	0.03	0.00	0.03	0.01	0.02	0.00	0.10	0.02	0.04	0.03
Total	88.37	87.27	86.99	87.62	92.07	92.35	93.58	92.58	93.21	92.66	93.13	93.87	92.68	92.85	93.11
Si	2.58	2.53	2.50	2.57	1.93	1.95	1.96	1.96	1.92	2.04	1.94	1.99	1.97	1.98	1.97
Al ^{IV}	1.42	1.47	1.50	1.43	-	-	-	-	-	-	-	-	-	-	-
Al ^{VI}	1.41	1.35	1.33	1.35	3.96	3.90	3.95	3.92	3.91	3.89	3.91	3.94	3.93	3.93	3.93
Ti	0.00	0.00	0.00	0.00	0.00	0.02	0.00	0.00	0.00	0.00	0.00	0.00	0.00	0.00	0.00
Fe ²⁺	1.52	1.43	1.41	1.46	1.64	1.68	1.66	1.67	1.49	1.67	1.65	1.40	1.39	1.42	1.46
Fe ³⁺	0.00	0.11	0.16	0.06	0.18	0.17	0.13	0.15	0.24	0.03	0.20	0.09	0.14	0.12	0.13
Mn	0.01	0.01	0.01	0.00	0.01	0.00	0.00	0.01	0.02	0.02	0.01	0.03	0.02	0.02	0.02
Mg	3.05	3.11	3.10	3.12	0.28	0.28	0.30	0.29	0.42	0.34	0.28	0.54	0.56	0.53	0.48
Ca	0.00	0.00	0.00	0.00	0.00	0.00	0.00	0.00	0.00	0.00	0.00	0.00	0.00	0.00	0.00
Ba	0.00	0.00	0.00	0.00	0.00	0.00	0.00	0.00	0.00	0.00	0.00	0.00	0.00	0.00	0.00
Na	0.01	0.00	0.00	0.00	0.00	0.00	0.00	0.00	0.00	0.00	0.00	0.00	0.00	0.00	0.00
K	0.01	0.00	0.00	0.01	0.00	0.00	0.00	0.00	0.00	0.00	0.00	0.01	0.00	0.00	0.00
Chlorite geothermometry															
KM(1987)	344.0	351.4	358.6	343.7											
C(1988)	395.7	407.1	417.6	395.7											
J(1991)	395.0	406.2	416.8	394.9											
X(1997)	394.7	406.2	416.5	395.0											

Table 3 – Bulk-rock composition from XRF analyses of the investigated samples, expressed in wt% of oxides.

Index mineral	Ms + Pg + Gr			Chl + Ms + Pg	Cld + Ms	
Name	R2	R14b	R22b	R15b	R6	R17
SiO ₂	79.67	85.67	80.49	50.07	79.37	81.06
TiO ₂	0.73	0.62	0.70	0.99	0.90	0.59
Al ₂ O ₃	10.97	8.98	10.99	20.80	12.07	10.10
FeO _{TOT}	3.07	0.22	2.16	7.75	2.95	3.31
MnO	0.01	0.00	0.01	0.11	0.01	0.02
MgO	0.77	0.10	0.28	3.54	0.29	0.27
CaO	0.14	0.01	0.07	3.58	0.02	0.01
Na ₂ O	0.41	0.43	0.88	1.32	0.19	0.15
K ₂ O	1.87	1.80	1.80	3.86	2.12	1.72
P ₂ O ₅	0.13	0.00	0.09	0.13	0.04	0.01
Sum	98.11	97.87	97.69	92.23	98.26	97.60

Table 4 – RSCM thermometry results on MRC samples, including number of spectra, mean R2 ratio (Beyssac et al., 2002) with standard deviation and mean estimated temperature with standard deviation.

<i>sample</i>	<i>n.spectra</i>	<i>R2</i>	<i>σ</i>	<i>T</i> (°C)	<i>σ</i> (°C)
R5	15	0.60	0.02	374.24	8.19
R1	13	0.59	0.01	376.38	5.88
R16b	13	0.57	0.02	386.42	7.68
R7c	10	0.60	0.02	373.09	7.92
R13	11	0.59	0.02	379.65	6.86
R19	9	0.56	0.02	390.32	9.80
R2	9	0.60	0.06	375.41	8.79
R9	15	0.57	0.02	385.36	10.87
R15c	10	0.56	0.02	390.16	9.34
R20	14	0.54	0.01	401.36	6.12
R22b	16	0.58	0.03	381.39	12.81
R23	14	0.58	0.04	379.39	7.39
R24	12	0.58	0.02	384.60	7.96
R29b	14	0.55	0.04	386.35	8.08
R27	10	0.60	0.02	367.37	5.06
R30	20	0.55	0.03	392.27	9.32
R28	16	0.60	0.02	372.89	9.28